CANCER

Multispectral fluorine-19 MRI enables longitudinal and noninvasive monitoring of tumor-associated macrophages

Davide Croci[1,2,3], Rui Santalla Méndez[1,2,3], Sebastian Temme[4,5], Klara Soukup[1,2,3], Nadine Fournier[3,6], Anoek Zomer[1,2,3], Roberto Colotti[7], Vladimir Wischnewski[1,2,3], Ulrich Flögel[5,8], Ruud B. van Heeswijk[9]†, Johanna A. Joyce[1,2,3]†*

High-grade gliomas, the most common and aggressive primary brain tumors, are characterized by a complex tumor microenvironment (TME). Among the immune cells infiltrating the glioma TME, tumor-associated microglia and macrophages (TAMs) constitute the major compartment. In patients with gliomas, increased TAM abundance is associated with more aggressive disease. Alterations in TAM phenotypes and functions have been reported in preclinical models of multiple cancers during tumor development and after therapeutic interventions, including radiotherapy and molecular targeted therapies. These findings indicate that it is crucial to evaluate TAM abundance and dynamics over time. Current techniques to quantify TAMs in patients rely mainly on histological staining of tumor biopsies. Although informative, these techniques require an invasive procedure to harvest the tissue sample and typically only result in a snapshot of a small region at a single point in time. Fluorine isotope 19 MRI (^{19}F MRI) represents a powerful means to noninvasively and longitudinally monitor myeloid cells in pathological conditions by intravenously injecting perfluorocarbon-containing nanoparticles (PFC-NP). In this study, we demonstrated the feasibility and power of ^{19}F MRI in preclinical models of gliomagenesis, breast-to-brain metastasis, and breast cancer and showed that the major cellular source of ^{19}F signal consists of TAMs. Moreover, multispectral ^{19}F MRI with two different PFC-NP allowed us to identify spatially and temporally distinct TAM niches in radiotherapy-recurrent murine gliomas. Together, we have imaged TAMs noninvasively and longitudinally with integrated cellular, spatial, and temporal resolution, thus revealing important biological insights into the critical functions of TAMs, including in disease recurrence.

INTRODUCTION

The brain tumor microenvironment (TME) is composed of malignant cancer cells, tissue-resident and peripherally recruited immune cells, stromal cells, astrocytes, and neurons, along with noncellular components, that collectively orchestrate tumor development and modulate the response to anticancer treatments (*1*, *2*). The precise composition and phenotypes of immune cells in the brain TME is dictated by several parameters, including the intracranial or extracranial origin of the tumor, the genetic drivers of the cancer, and the type of therapeutic intervention (*3*–*5*).

The most aggressive primary brain tumors in adults are high-grade gliomas, also termed glioblastomas (*6*). Despite treatment with standard-of-care therapy, which includes surgical resection, radiotherapy (RT), and chemotherapy with the alkylating agent temozolomide (TMZ), median survival remains just 14 months after diagnosis, and the 5-year survival is less than 5% (*7*). Recent comprehensive analyses of the immune cell composition of diverse brain malignancies in patients, including low- and high-grade gliomas, and brain metastases originating from different primary cancers revealed disease-specific alterations in both immune cell abundance and functions (*3*, *4*). The immune microenvironment of high-grade gliomas was found to be predominantly populated by tumor-associated macrophages (TAMs) comprising brain-resident microglia (MG) and monocyte-derived macrophages (MDMs) that were recruited from the peripheral circulation (*3*, *4*). Standard-of-care therapies, including RT and TMZ, have been shown to directly alter the TME composition, with pronounced effects on myeloid cells in particular (*5*, *8*). Time course analyses, incorporating several fixed time points, showed that the relative abundance and phenotypes of MG and MDMs changed in response to RT in multiple genetically distinct murine glioma models (*5*). Combining RT with therapeutic targeting of TAMs by colony-stimulating factor-1 receptor (CSF-1R) inhibition to "reeducate" these cells, or by depletion of MDMs, resulted in a prolonged survival of tumor-bearing animals (*5*). CSF-1R inhibition has been shown to be a promising and translationally relevant approach in several preclinical studies using models of diverse brain cancers (*5*, *9*–*14*), and clinical trials with a potent CSF-1R inhibitor (BLZ945) are ongoing in patients with advanced cancer, including gliomas (NCT02829723) (*15*). The evolving TME was also recently assessed in response to TMZ chemotherapy, which revealed specific myeloid cell dynamics during tumor progression and upon treatment in distinct models of mesenchymal and proneural glioma (*8*).

[1]Department of Oncology, University of Lausanne, Lausanne 1011, Switzerland. [2]Ludwig Institute for Cancer Research, University of Lausanne, Lausanne 1011, Switzerland. [3]Agora Cancer Research Center, Lausanne 1011, Switzerland. [4]Department of Anesthesiology, Universitätsklinikum Düsseldorf, Heinrich-Heine-Universität, Düsseldorf 40225, Germany. [5]Experimental Cardiovascular Imaging, Universitätsklinikum Düsseldorf, Heinrich-Heine-Universität, Düsseldorf 40225, Germany. [6]Bioinformatics Core Facility, SIB Swiss Institute of Bioinformatics, Lausanne 1011, Switzerland. [7]In Vivo Imaging Facility (IVIF), Department of Research and Training, Lausanne University Hospital and University of Lausanne, Lausanne 1011, Switzerland. [8]Institute for Molecular Cardiology, Universitätsklinikum Düsseldorf, Heinrich-Heine-Universität Düsseldorf, Düsseldorf 40225, Germany. [9]Department of Radiology, Lausanne University Hospital and University of Lausanne, Lausanne 1011, Switzerland.
†Co-senior authors.
*Corresponding author. Email: johanna.joyce@unil.ch

Dynamic monitoring of the cells of the brain TME is therefore crucial to fully understand both disease biology and response to treatment. Although TAMs can be analyzed using a multitude of experimental techniques in preclinical models, TAM quantification in patients currently relies mainly on histological staining of tumor biopsies. This approach has several limitations, including the fact that biopsies only represent a small portion of the entire tumor and thus do not necessarily capture the full tissue heterogeneity. Moreover, surgical access to the brain is challenging, which does not facilitate frequent and repeated sampling to follow cellular dynamics over time. It is therefore essential to develop new technological strategies that will enable the noninvasive and longitudinal monitoring of multiple aspects of the disease, including changes in the TME composition.

Magnetic resonance imaging (MRI) is a widely used and indispensable imaging modality in neuro-oncology, where it enables key decision-making steps including tumor diagnosis, precise guidance for planning surgery and targeted RT, and monitoring the subsequent response to treatment (*16*). Historically, MR images have been primarily used for a qualitative and objective assessment of the tumor by clinicians. However, recent neuroimaging advances have contributed to the development of quantitative and molecular MRI techniques (*17*–*19*), which have the potential to transform the interpretation and application of imaging results into routine clinical practice. Nonetheless, research into fully quantitative MRI-based biomarkers of glioma is still very much an ongoing endeavor. The major challenges include the technical, biological, and clinical validation of such biomarkers to implement robust imaging methods that will enable the acquisition of multiparametric information, including TME-centered data (*16*).

The clinical application of macrophage imaging requires safe and biocompatible targeting agents and an accurate and precise interpretation of the resulting signal. Several MRI-based noninvasive molecular imaging techniques fulfill these conditions for a potentially powerful strategy to visualize myeloid cells (*20*, *21*). Among these, isotope fluorine-19 MRI (^{19}F MRI) takes advantage of perfluorocarbon-containing nanoparticles (PFC-NP), such as perfluoro-crown-ether (PFCE) or perfluoro-tert-butylcyclohexane (PFTBH) (*22*, *23*), and has been mostly used for nonneurological applications to date (*24*, *25*). PFCs are biologically inert organic compounds that are highly enriched in the stable isotope ^{19}F. The ^{19}F isotope is not naturally present in the body, and the ^{19}F signal is completely independent of the hydrogen signal normally used for routine MRI (^{1}H MRI). Thus, ^{19}F MRI enables a precise signal detection and quantification upon the injection of PFC-NP. Myeloid cells generally have a high capacity for phagocytosis, and their

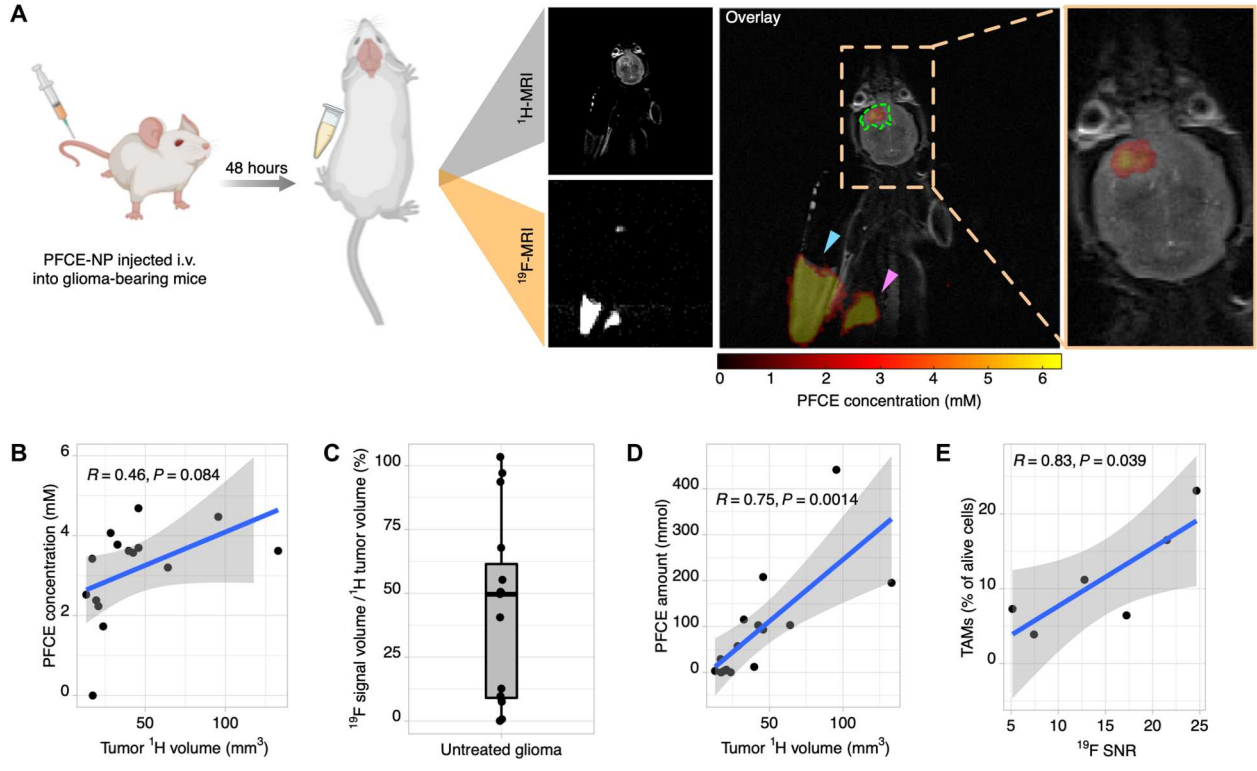

Fig. 1. ^{19}F MRI allows the noninvasive imaging of glioma-associated inflammation. (**A**) ^{19}F MR imaging workflow: PDG-Ink4a/Arf KO glioma-bearing mice were injected with PFCE-NP and then imaged 48 hours later by conventional ^{1}H MRI to visualize the anatomical location of the tumor, in addition to molecular ^{19}F MRI. The overlay (right) shows the ^{19}F signal evident in the tumor (green dashed line), but not in the contralateral healthy brain, in the liver (pink arrowhead) and in a PFCE-NP–containing reference tube (cyan arrowhead) placed adjacent to the mouse, which allows the absolute quantification of the tumor signal into a PFCE amount or concentration. i.v., intravenous. (**B**) Correlation of the PFCE concentration and ^{1}H tumor volume. (**C**) Percentage of ^{19}F signal coverage of the total tumor ^{1}H volume. (**D**) Correlation of the total PFCE amount and ^{1}H tumor volume. (**E**) Correlation of the ^{19}F signal-to-noise ratio (SNR) with the abundance of tumor-associated macrophages (TAMs) (CD45$^+$ CD11b$^+$ Ly6G$^-$ Ly6C$^-$) quantified by flow cytometry. PDG-Ink4a/Arf KO model: n = 15 mice. Regression analysis was done using a linear model.

uptake of PFC-NP has been used as a readout for inflammation-related processes (*24*–*27*). Because of the critical role of TAMs in regulating tumor biology and influencing therapeutic response, we decided to investigate ^{19}F MRI as a strategy to noninvasively longitudinally monitor TAMs in vivo in experimental mouse models of gliomagenesis, breast-to-brain metastasis (BrM), and primary breast cancer. In this study, we report the successful tracking of different TAM populations with integrated cellular, spatial, and temporal resolution, which has allowed us to reveal biological insights into the dynamic evolution of the TME. This study also serves to highlight the potential of in vivo ^{19}F MRI to ultimately complement, or perhaps even replace, the existing histological-based assessment of TAMs in patient samples.

RESULTS

Multiparametric MRI reveals a tumor-restricted accumulation of PFCE-NP in preclinical models of multiple cancers

We began by assessing whether multiparametric ^{1}H and ^{19}F MRI can be used in conjunction for molecular imaging of several preclinical cancer models. We first analyzed a genetically engineered mouse model (GEMM) of gliomagenesis, in which nestin-positive neural progenitor cells overexpress the oncogenic platelet-derived growth factor–β (PDGF-β) by taking advantage of the transgenic RCAS-tva delivery strategy (*28*). High-grade gliomas develop in a highly penetrant manner when this model is crossed into an *Ink4a/Arf* tumor suppressor–deficient background [termed PDG-Ink4a/Arf knockout (KO) GEMM] (*5*, *11*, *28*–*30*). Tumor-bearing mice were injected with a PFCE-NP emulsion and imaged 48 hours later using a 3T clinical MRI scanner (Prisma, Siemens) equipped for both ^{1}H and ^{19}F sequential imaging (Fig. 1A). We detected a robust ^{19}F signal and PFCE accumulation inside the gliomas, which were anatomically defined by standard ^{1}H MRI (Fig. 1B). By contrast, the contralateral healthy brain, as well as the brain of control nontumor bearing mice, did not show any ^{19}F signal (fig. S1A). The measured PFCE concentrations were above the detection limit of PFCE at 3T (fig. S1B). Brain tumors can display diverse anatomical features by ^{1}H MRI, which may indicate functionally discrete regions (*31*). We therefore analyzed the extent of the ^{19}F distribution in detail and found that the proportion of the total tumor volume covered by the ^{19}F signal varied considerably and showed distinct patterns in different animals (Fig. 1C and fig. S1C). We also observed PFCE accumulation in the liver (Fig. 1A and fig. S1A), in agreement with a previous description of its function in PFCE uptake and excretion (*22*). Therefore, the ability to assess whole-body ^{19}F distribution in vivo in this manner represents an important advance over the recently reported static ex vivo ^{19}F MRI of a glioma model that was generated by intracranial injection of cancer cells (*32*).

We next asked whether this imaging strategy could also be applied to other brain cancer models and evaluated the ^{1}H-^{19}F MRI pipeline in a BrM mouse model, termed PyMT-BrM3. We generated the PyMT-BrM3 cell line from the sequential in vivo selection (three rounds) of a metastatic cell line that was originally derived from the MMTV-Polyoma Middle T-antigen (PyMT) mammary tumor model (BL/6 background). Intracardiac injection of PyMT-BrM3 cells in BL/6 mice leads to cancer cell circulation in the blood, extravasation, seeding, and outgrowth of multiple lesions throughout the brain parenchyma. By comparison with PDG-Ink4a/Arf KO gliomas, the ^{19}F coverage of the metastatic lesions was lower, as reflected by the lower PFCE concentration and amount in the PyMT-BrM3 model (fig. S1, D to F). Nonetheless, in both gliomas and brain metastases, there was a positive correlation between the total amount of PFCE and tumor volume as determined by ^{1}H MRI (Fig. 1D and fig. S1F). Primary breast tumor models have been reported to display a ^{19}F signal upon injection of PFC agents (*33*, *34*). We therefore investigated whether extracranial tumors might accumulate more PFCE-NP by injecting the PyMT-BrM3 cell line orthotopically in the mammary fat pad (termed "primary breast tumor" model). Upon ^{19}F MR imaging, we indeed found a higher PFCE accumulation than in the corresponding brain metastatic lesions (fig. S1G), indicating that properties of the brain or the brain TME might affect the PFCE-NP uptake. Together, these results demonstrate that multiparametric MRI is technically feasible in vivo in different preclinical cancer models and can be used to reveal valuable molecular information in addition to conventional ^{1}H MRI. The heterogeneous ^{19}F pattern observed in the glioma and BrM models and the higher total amount of PFCE in larger brain tumors, as well as in extracranial tumors, suggest that a specific cellular composition and functionally distinct regions within the tumor could potentially underlie the ^{19}F signal distribution, which we subsequently investigated in detail.

We first asked whether the ^{19}F signal-to-noise ratio (SNR) correlated with the presence of any specific cell population, which was assessed by flow cytometry analysis of the cellular composition of the tumor. We found that myeloid cell abundance, in general, and TAMs, specifically, correlated positively with the ^{19}F SNR (Fig. 1E and fig. S1H), which was opposite to the abundance of nonimmune cells (fig. S1I). To determine whether there was a direct dependency of the ^{19}F SNR with macrophage abundance, we measured the ^{19}F signal in primary breast tumors that were treated with BLZ945, an anti-CSF1R inhibitor which has previously been shown to deplete macrophages in similar models (*35*, *36*). We found a lower ^{19}F SNR after in vivo treatment of tumor-bearing mice (fig. S1J). Together, these results indicate that the ^{19}F signal represents a direct readout of macrophage abundance, and we subsequently investigated the exact cellular source and accumulation of the PFCE-NP.

PFCE-NP accumulate in tumor-associated MG and macrophages in gliomas, enabling their specific imaging by ^{19}F MRI

^{19}F MRI has been used in different models of inflammatory disease, where myeloid cells at the site of inflammation have been shown to take up injected PFC-NP (*25*, *34*, *37*). However, this powerful imaging approach has not yet been widely applied to assess the dynamics of cancer-associated inflammation in vivo. Brain tumor development and progression can result in heterogeneous breakdown of the blood-brain barrier (BBB), facilitating the entry of peripheral immune cells, mainly of myeloid origin, which, along with the various brain-resident cells, contribute to form a complex and diverse brain TME (*1*–*4*). We therefore assessed the exact cellular source of the ^{19}F signal that we observed in the PDG-Ink4a/Arf KO GEMM. To do so, we injected glioma-bearing mice with fluorescent rhodamine–labeled PFCE-NP (rhodamine-PFCE-NP), allowed the NP to circulate for 24 hours, and analyzed the cellular composition of the tumors by flow cytometry at the end of the

experiment. We observed a high abundance of myeloid cells in gliomas (fig. S2A), as previously described for this mouse model (*5*, *11*, *28*–*30*) and similar to analyses of patient samples (*3*, *4*). In our flow cytometry analysis, specifically investigating the rhodamine-PFCE-NP$^+$ cells (Fig. 2A and fig. S2B), we found that myeloid cells accounted for the majority of positive cells. TAMs, together with a smaller proportion of monocytes, constituted the rhodamine-PFCE-NP$^+$ myeloid pool (Fig. 2, B and C). Although we also detected rhodamine-PFCE-NP in some nonimmune cells by flow cytometry, the median fluorescence intensity (MFI) of rhodamine was substantially higher in both resident MG and recruited MDMs (Fig. 2D), indicating a substantial enrichment of NP specifically in these cells. TAMs have been shown to represent a very heterogeneous cellular population (*38*). We therefore investigated in detail the granularity of the TAM compartment with relation to the rhodamine-PFCE-NP uptake by performing t-distributed stochastic neighbor embedding (tSNE) analysis of the flow cytometry data (Fig. 2E). We identified both MG and MDM populations, defined by differential expression of CD49d and CD45 (*29*), which were additionally clustered in subpopulations characterized by the differential expression of the major histocompatibility complex II (MHCII), CD11c, CD64, and F4/80. We found that the majority of the MHCII$^+$ CD11c$^+$ CD64$^-$ F4/80$^-$ cells were enriched in the rhodamine-PFCE-NP–negative fraction, indicating no uptake by this population (fig. S2C). To evaluate any extracellular deposition or accumulation of the NP, we also analyzed tissue sections by immunofluorescence (IF) staining with the pan-macrophage marker Iba1 and staining of all cell membranes using the wheat germ agglutinin (WGA) (Fig. 2F). We observed NP accumulation within Iba1$^+$ macrophages, whereas no extracellular deposition was detected (Fig. 2G). These data corroborated our finding that the ^{19}F SNR correlated with a high abundance of TAMs in gliomas (Fig. 1E).

We then assessed the proportion of rhodamine-PFCE-NP$^+$ cells in a cell type–specific manner (Fig. 2H, and fig. S2, D and E). We found that although myeloid cells represented the major rhodamine-PFCE-NP$^+$ population, only a small percentage within the different cell populations accumulated the rhodamine-PFCE-NP. A higher frequency of rhodamine-PFCE-NP$^+$ cells was observed in TAMs compared to monocytes (Fig. 2H), and uptake by cells of lymphoid origin or nonimmune cells was generally low (fig. S2E). CD31$^+$ endothelial cells showed a slightly higher frequency of rhodamine-PFCE-NP$^+$ cells compared to other nonimmune cells (fig. S2E), which could indicate a role for the vasculature in the distribution of the NP, as discussed below. Given that the TME composition can change dynamically over time, partly as a consequence of the infiltration of newly recruited immune cells from the periphery, we also assessed the uptake of rhodamine-PFCE-NP in myeloid cells isolated from the blood and the bone marrow. However, we did not observe substantial accumulation of the compound in these tissues (fig. S2F) and thus consider it unlikely that cells recruited de novo from outside the brain would substantially affect the ^{19}F signal in the days after PFCE-NP injection. Together, we were able to identify TAMs as the major cellular contributor to the pool of rhodamine-PFCE-NP$^+$ cells, showing both a higher accumulation and MFI signal compared to the other cell types analyzed. Therefore, we conclude that TAMs are the major source of the ^{19}F signal detected by MRI.

PFCE-NP accumulate in proximity to dysmorphic vessels

MR imaging revealed a ^{19}F signal localized to the tumor mass and not in the contralateral healthy brain, suggesting the presence of an inflammatory microenvironment specifically in the diseased tissue area. Similarly, we did not observe any rhodamine-PFCE-NP uptake in the contralateral tumor-free brain (fig. S2G). Whereas MG isolated from both the tumor and the normal contralateral brain were both capable of taking up the rhodamine-PFCE-NP ex vivo in cell culture (Fig. 2I and fig. S2H), CD45$^+$ CD11b$^-$ lymphocytes were not (fig. S2I). This indicates that the absence of uptake in vivo in the contralateral brain could be related to the NP distribution rather than differences in the phenotypes or phagocytic capabilities of the MG. Although the BBB protects the brain from entry of exogenous substances and pathogens under normal homeostasis, thereby constituting a potential hurdle for PFCE-NP distribution, it can be compromised in brain malignancies (*39*). Given the small percentage of cells showing accumulation of the rhodamine-PFCE-NP (Fig. 2H and fig. S2E), the absence of uptake in the contralateral brain in vivo (fig. S2G), and the heterogeneous ^{19}F signal within the tumor (Fig. 1C), we reasoned that the abnormal nature of the brain tumor vascular network could affect the differences in observed PFCE-NP distribution. To investigate this further, we induced PDG-Ink4a/Arf KO gliomas that were green fluorescent protein positive (GFP$^+$) , thereby enabling precise visualization of the tumor mass, and investigated the distribution pattern of rhodamine-PFCE-NP. To image the vasculature, we injected DyLight649-fluorescent lectin intravenously and allowed it to circulate for 5 min before euthanizing the mouse. IF analysis showed that the rhodamine-PFCE-NP$^+$ Iba1$^+$ cells localized in the vicinity of the vessels (fig. S3, A and B). We therefore investigated whether this accumulation was related to specific morphological properties of the tumor vasculature. To retain the three-dimensional (3D) structure of the vessels, and because the rhodamine-PFCE-NP signal can be sensitive to degradation posttissue processing (*40*), we imaged freshly cut 425-μm-thick tissue slices ex vivo with a two-photon microscope, immediately after harvesting and slicing of the brain. We observed a heterogeneous pattern of NP accumulation, whereby distinct regions within the same tumor showed a differential distribution of the rhodamine signal (Fig. 3A).

We reconstructed the imaged slices using the analysis software Imaris (fig. S3C) and first assessed whether the accumulation was similar to the flow cytometry results discussed above. We found that only a minor proportion of the rhodamine$^+$ foci were also GFP$^+$ (indicating tumor cells) (fig. S3D), and similarly, only a small percentage of GFP$^+$ cells showed a rhodamine signal (fig. S3E). We then examined how the tumor vasculature might affect the degree of accumulation of the rhodamine-PFCE-NP. Image reconstruction using Imaris enabled a multiparametric analysis of the tumor vessels, including vessel dendrite morphology, orientation, and branching (fig. S3F). A principal components analysis of all vascular morphological parameters showed the independent clustering of rhodamine^{HIGH} areas (with respect to the healthy brain parenchyma) (Fig. 3B). Together, these analyses revealed a heterogeneous vascular morphology within the tumors, ranging from "healthy brain-like" vessels to a completely dysmorphic vasculature, which precisely correlated with the amount of rhodamine-PFCE-NP accumulation (Fig. 3B).

We then sought to longitudinally assess the kinetics of rhodamine-PFCE-NP distribution by taking advantage of a recently

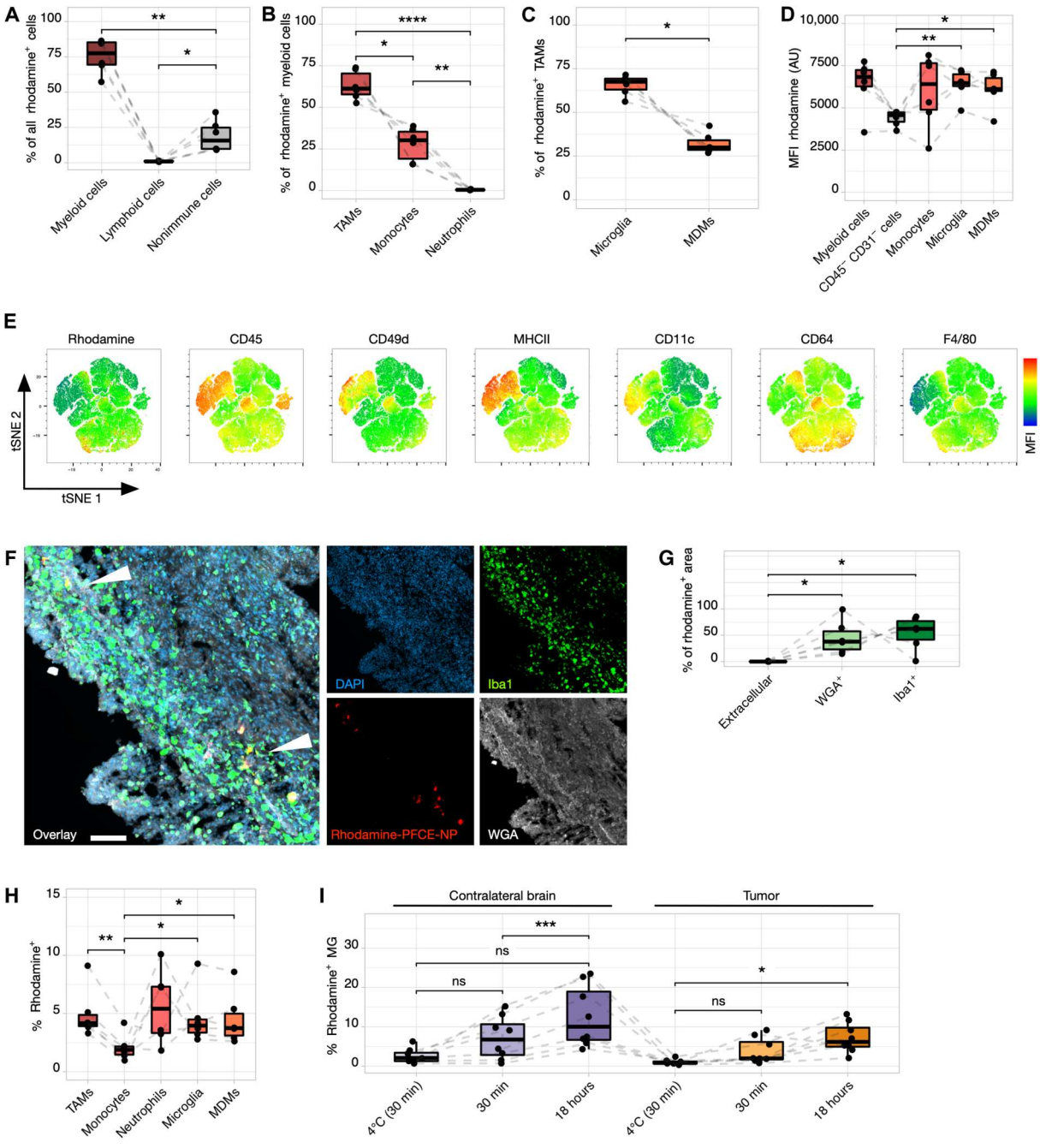

Fig. 2. PFCE-NP cellular accumulation predominantly occurs in the TAM compartment. (**A**) Flow cytometry characterization of the fluorescent rhodamine-labeled PFCE-NP–positive (rhodamine-PFCE-NP$^+$) cell pool in PDG-Ink4a/Arf KO gliomas, showing a higher proportion of the myeloid compartment (CD45$^+$ CD11b$^+$ cells) than nonimmune cells (CD45$^-$ CD11b$^-$) and lymphoid cells (CD45$^+$ CD11b$^-$) (n = 6 mice). (**B**) Depiction of all rhodamine-PFCE-NP$^+$ myeloid cells showing TAMs (CD45$^+$ CD11b$^+$ Ly6G$^-$ Ly6C$^-$), monocytes (CD45$^+$ CD11b$^+$ Ly6G$^-$ Ly6C$^+$), and neutrophils (CD45$^+$ CD11b$^+$ Ly6G$^+$ Ly6C$^+$) (n = 6 mice). (**C**) Delineation of rhodamine-PFCE-NP$^+$ TAMs between microglia (MG) (CD49d$^-$) and monocyte-derived macrophages (MDMs) (CD49d$^+$) (n = 6 mice). (**D**) Median fluorescence intensity (MFI) of the rhodamine signal in the different myeloid cell types and CD45$^-$ CD31$^-$ cells (n = 6 mice). AU, arbitrary units. (**E**) t-distributed stochastic neighbor embedding (tSNE) analysis of TAMs (CD45$^+$ CD11b$^+$ Ly6G$^-$ Ly6C$^-$). Flow cytometry data show the expression of different cell surface markers. The tSNE analysis was based on the markers CD45, CD11b, Ly6G, Ly6C, CD49d, MHCII, CD11c, CD64, and F4/80 (n = 6 mice, pooled). (**F**) Representative immunofluorescence (IF) image of glioma tissue showing 4′,6-diamidino-2-phenylindole (DAPI)–labeled cell nuclei (blue), the pan-macrophage marker Iba1 (green), rhodamine-PFCE-NP (red), and cell membrane staining with wheat germ agglutinin (WGA; white). White arrowheads indicate double-positive Iba1/rhodamine-PFCE-NP cells. Scale bar, 100 μm. (**G**) Quantification of the IF images showing the percentage of the total rhodamine$^+$ area in each cellular and noncellular compartment (n = 6 mice). (**H**) Quantification of the percentage of rhodamine-PFCE-NP$^+$ cells of total cells in the different myeloid populations (n = 6 mice) as measured by flow cytometry. (**I**) Quantification of rhodamine-PFCE-NP$^+$ MG (CD45$^+$ CD11b$^+$ Ly6G$^-$ Ly6C$^-$ CD49d$^-$) after ex vivo treatment of dissociated contralateral brains and matched tumors (n = 8 mice). *P < 0.05, **P < 0.01, ***P < 0.001, ****P < 0.0001, not significant (ns) if not otherwise stated; data were analyzed using a post hoc Tukey's multiple comparisons test. Data in (C) were analyzed using a paired Wilcoxon test.

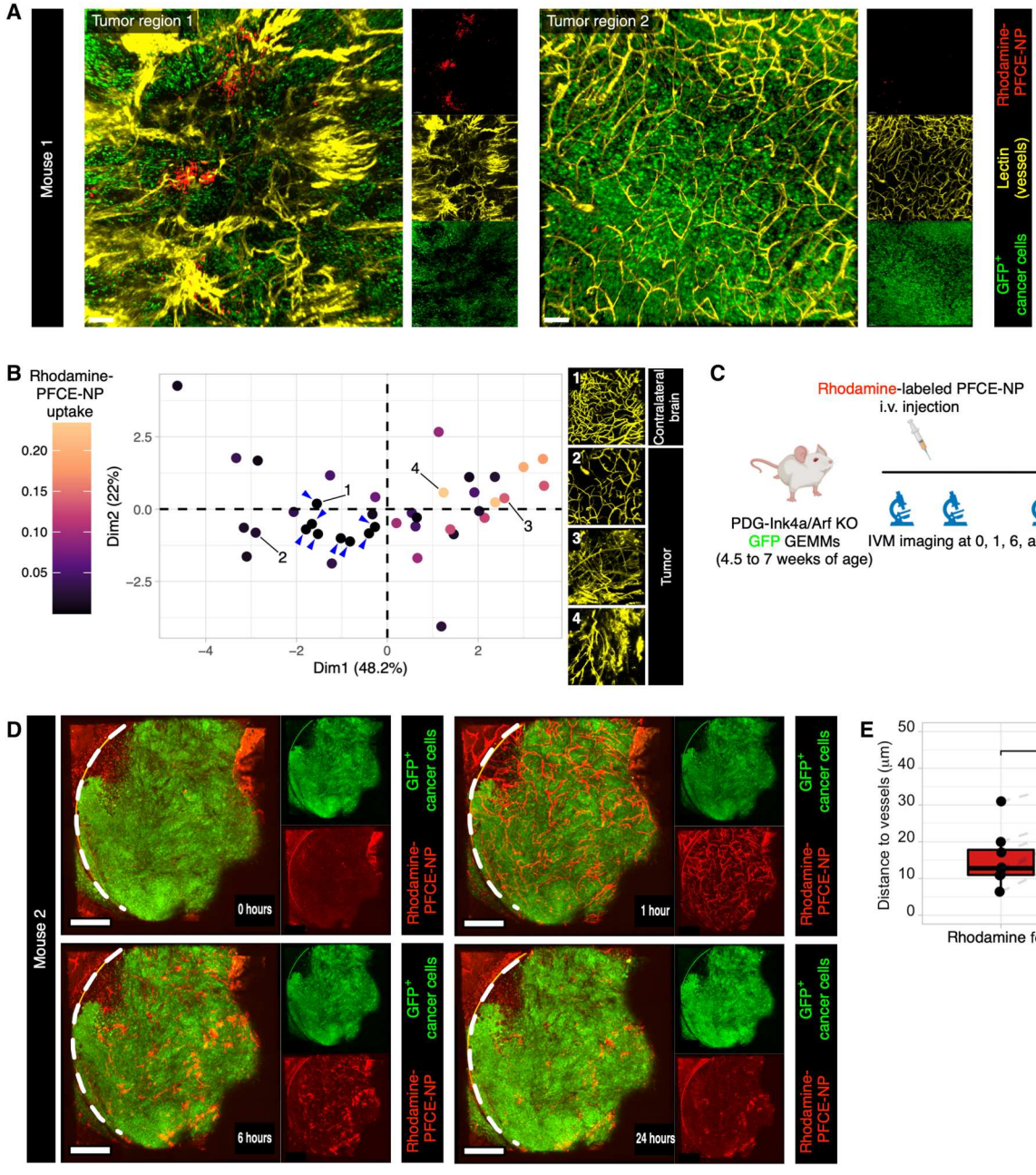

Fig. 3. PFCE-NP accumulate in proximity to dysmorphic vessels. (**A**) Representative two-photon microscopy images of brain slices showing GFP-expressing cancer cells (green), the DyLight649-lectin–labeled vasculature (yellow), and rhodamine-PFCE-NP$^+$ foci (red) in two distinct areas of the same tumor. Scale bar, 100 μm. (**B**) Principal components analysis based on nine different vessel parameters (*Z*-score normalized) of different volume of interest (VOI) (3 to 6 VOI per mouse; $n = 8$) in different tumor areas and healthy contralateral brain adjacent to the tumor (blue arrowheads). The color bar shows the rhodamine-PFCE-NP uptake (total rhodamine$^+$ foci volume normalized to the total VOI volume). Images 1, 2, 3, and 4 show representative VOIs of the vascular morphology in the healthy contralateral brain (*1*) and the tumor (2 to 4, ranked by rhodamine-PFCE-NP uptake). (**C**) Experimental design for intravital microscopy (IVM): GFP-PDG-Ink4a/Arf KO glioma-bearing were imaged before rhodamine-PFCE-NP administration ($t = 0$ hours) and 1, 6, and 24 hours later. (**D**) Longitudinal imaging of the same glioma-bearing mouse by two-photon microscopy through a cranial imaging window (CIW; white dashed line). Representative images of the glioma area below the CIW were taken at different time points before ($t = 0$ hours) and after ($t = 1$, 6, and 24 hours) injection of the rhodamine-PFCE-NP, initially showing the circulation of the NP in the bloodstream ($t = 1$ hour) followed by a gradual accumulation of rhodamine$^+$ foci in the tumor ($t = 6$ and 24 hours). Scale bars, 500 μm. (**E**) Quantification of the average distance to the DyLight649-lectin$^+$ vessels of rhodamine-PFCE-NP$^+$ foci and all GFP-positive cancer cells, respectively ($n = 8$ mice). $^{**}P < 0.01$, as determined by a paired Wilcoxon test.

established intravital microscopy (IVM)–MRI pipeline in living animals (*41*). We induced GFP$^+$ tumors in the PDG-Ink4a/Arf KO GEMM, where a cranial imaging window (CIW) was surgically implanted in the skull at the site of tumor induction. After tumor detection by conventional ^{1}H MRI, mice were imaged by two-photon microscopy enabling longitudinal live imaging within the GFP$^+$ tumor area precisely below the CIW (Fig. 3C). Immediately after injection of the rhodamine-PFCE-NP, we analyzed the dynamics of the rhodamine signal inside the blood vessels, which were highlighted by the circulating fluorescent NP (Fig. 3D and fig. S3G). We found that the rhodamine signal was almost completely cleared from the blood circulation 6 hours after NP injection. In line with our results above showing a heterogeneous pattern of rhodamine$^{LOW/HIGH}$ regions, we were able to detect a clear signal in vivo directly below the CIW in 2 of 11 mice that were imaged (Fig. 3D and movies S1 to S3).

Given the higher NP uptake in regions with dysmorphic vessels, we next sought to address whether the NP were subsequently distributed effectively from the circulation into the tumor mass. We thus analyzed the distance of the rhodamine$^+$ foci to the vessels (and GFP$^+$ cancer cells to the vessels) in tumor-bearing brain slices and found that NP accumulated in proximity to the vasculature (Fig. 3E). GFP$^+$ cancer cells with a detectable rhodamine signal were also closer to the vessels compared to rhodamine-negative cancer cells (fig. S3H). Because the positioning of TAMs relative to the vasculature potentially affects their phenotype and oxidative metabolism (*42*), we asked whether the specific distribution pattern of rhodamine-PFCE-NP$^+$ TAMs could reflect a precise subpopulation. We therefore used fluorescence-activated cell sorting to collect rhodamine-PFCE-NP$^+$ and rhodamine-PFCE-NP$^-$ TAMs, respectively, and performed RNA sequencing (RNA-seq) (fig. S4A). TAMs were gated as CD45$^+$ CD11b$^+$ Ly6G$^-$ Ly6C$^-$ cells to obtain a broad overview of the population-based phenotypes rather than focusing too narrowly on isolating each of the different subpopulations identified by flow cytometry (Fig. 2E). In line with their perivascular location, gene set enrichment analysis (GSEA) revealed a higher oxidative phosphorylation activity in the rhodamine-PFCE-NP$^+$ population (Fig. 4A), consistent with an altered metabolism. Moreover, GSEA network analysis showed an enrichment of several mitochondrial components (Fig. 4B) and central enzymes of the tricarboxylic acid cycle, including *Dlat*, *Idh1*, and *Idh2* (Fig. 4C). To validate the RNA-seq results, we stained glioma tissue sections by IF for the macrophage marker CD68 and the metabolic enzyme IDH2 (Fig. 4D). We identified two TAM subpopulations: a IDH2$^+$ subset in proximity to CD31$^+$ endothelial cells and a larger proportion of IDH2$^-$ TAMs, which were more distant from the vessels (Fig. 4E and fig. S4B). Together, these results indicate that rhodamine-PFCE-NP$^+$ TAMs are characterized by an oxidative metabolic signature, including high *Idh2* expression, and are localized within perivascular niches.

^{19}F MRI allows the noninvasive and longitudinal monitoring of TAMs in gliomas after RT

We next asked whether ^{19}F MRI could be used to monitor changes in the TME after therapeutic intervention in a noninvasive and longitudinal manner. RT is part of the standard-of-care therapy for patients with glioma (*7*) and has been shown to alter the composition of the glioma TME (*5*, *38*). Time course analyses of fixed time points previously revealed that the overall abundance and phenotypes of TAMs were substantially affected by RT, in addition to alterations in the relative proportions of recruited MDMs versus brain-resident MG (*5*). Although PFCE-NP uptake occurred in a subset of TAMs at baseline, as shown in our analyses above, we sought to address whether this population would be indicative and representative of general TAM dynamics after RT. We therefore first injected glioma-bearing mice with a single dose of PFCE-NP, which has been previously reported to be slowly cleared from the liver (*22*), to specifically track the dynamics of the initial TAM pool only. Mice were then imaged by ^{1}H and ^{19}F MRI to determine the baseline PFCE concentration and tumor volume before RT and subsequently imaged weekly until tumor recurrence (Fig. 5A).

Single-dose RT treatment led to an initial tumor regression, followed by a quiescent phase, and eventually, all tumors relapsed (Fig. 5B). First, we analyzed TAM dynamics by IF after RT treatment (single dose of 10 Gy) (Fig. 5C). Consistent with previous reports using fractionated RT (*5*), we found a transient increase in the abundance of all TAMs after single-dose RT, with a peak at 7 days after treatment (Fig. 5C). We then quantified the PFCE concentration over time, in a separate cohort, and found a significant increase 7 days after RT ($P < 0.001$; Fig. 5D), consistent with the observed abundance of TAMs by IF staining (Fig. 5C). Normalization of the tumor PFCE concentration to the liver PFCE concentration, as a measure of potential compound clearing, confirmed the increase after RT (fig. S5A). The total PFCE amount normalized to the ^{1}H tumor volume also increased after treatment (fig. S5B). The PFCE concentration was stable in the liver over the full time course, indicating a very slow clearance of PFCE (fig. S5, C and D), consistent with previous reports (*22*). Moreover, we did not observe changes in the amount of PFCE inside the tumor (fig. S5E), indicating a cellular labeling only after compound administration, in line with our results from flow cytometry and IVM that showed no peripheral PFCE-NP uptake and a rapid clearance from the bloodstream (figs. S2F and S3G). Overall, these results demonstrated that ^{19}F MRI can be used to track the initial TAM dynamics at 7 days after RT treatment.

We also investigated whether the changes in the ^{19}F signal over the full trial length could be indicative of the long-term TAM dynamics that we observed by IF staining at different time points (Fig. 5C), where overall TAM abundance returns to baseline at tumor recurrence. First, we addressed whether the tumor PFCE concentration returned to the initial concentrations in the subset of mice that could be imaged until 28 days after RT (not all treated animals survived to this time point) (fig. S5F), but no reduction was detected (fig. S5F). Moreover, we observed a decreased total PFCE amount in the tumor, probably related to local clearing (fig. S5G). Together, these results showed that after an initial precise monitoring of the RT-mediated TAM increase, long-term ^{19}F MRI did not enable a comprehensive assessment of TAM dynamics over the full time course of the trial, and we therefore sought to use additional approaches to address this further.

Multispectral ^{19}F MRI identifies spatial and temporally distinct cellular populations in RT recurrent tumors

Previous findings in the context of fractionated RT revealed a shift in the MDM to MG ratio in recurrent tumors by flow cytometry analysis (*5*). However, the spatial distribution of these cell populations has not been investigated to date. To evaluate TAM changes during the complete duration of the trial, we began by analyzing the

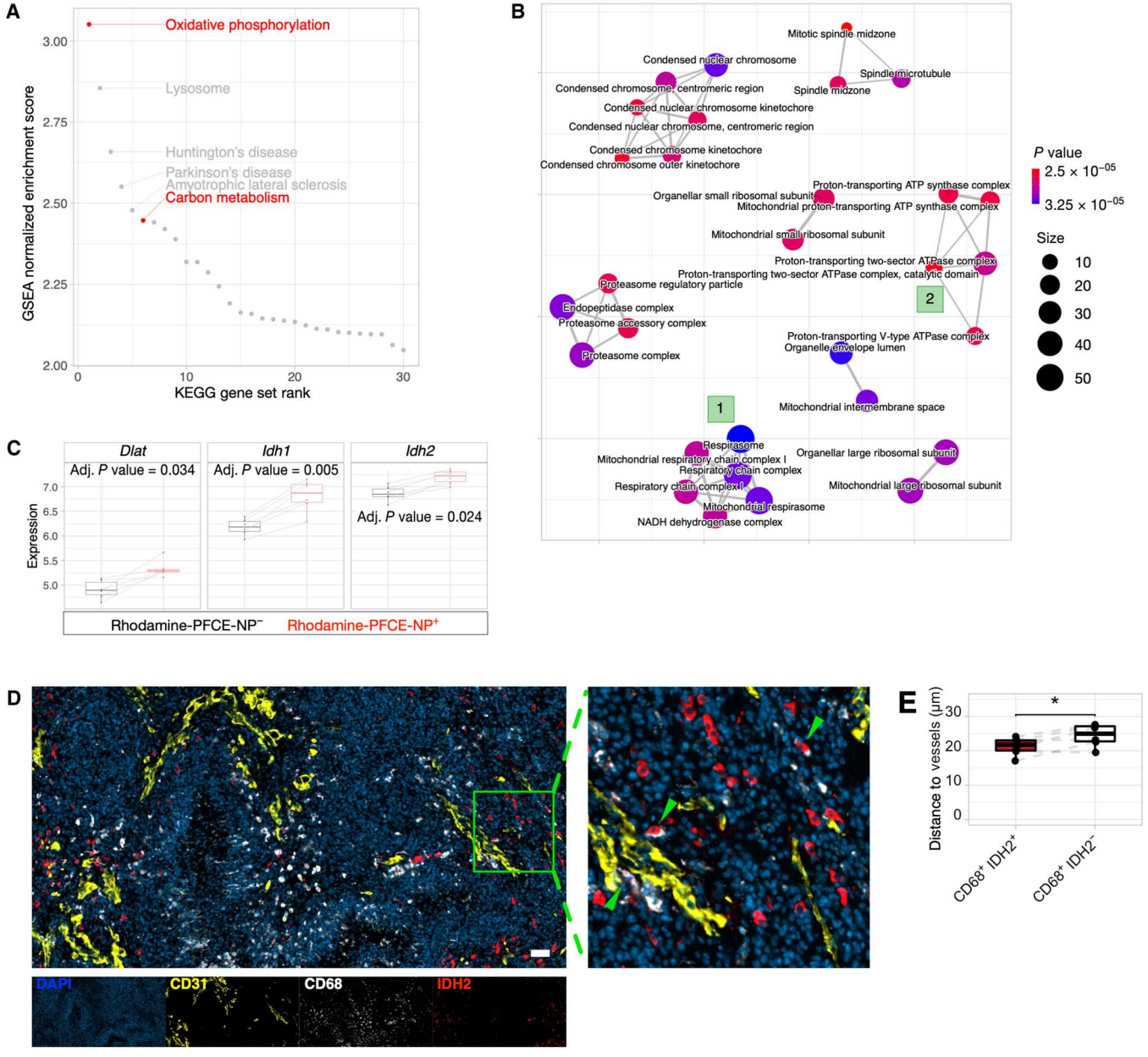

Fig. 4. PFCE-NP label a TAM subpopulation associated with high oxidative metabolic potential. (**A**) Gene set enrichment analysis (GSEA) shows an enrichment of oxidative metabolism–related pathways in the rhodamine-PFCE-NP$^+$ TAMs [Kyoto Encyclopedia of Genes and Genomes (KEGG) pathway database]. (**B**) GSEA network analysis of the top 30 enriched cellular components in the rhodamine-PFCE-NP$^+$ TAMs (GO cellular component database), showing different clusters, including several pathways involved in mitochondrial oxidative respiration (clusters "1" and "2" in the green squares). The dot size represents the gene set size, and the color bar indicates the *P* value. ATP, adenosine 5′-triphosphate; ATPase, adenosine triphosphatase; NADH, reduced form of NAD$^+$. (**C**) Box plots depicting normalized $\log_2$ gene expression values for *Dlat*, *Idh1*, and *Idh2* in rhodamine-PFCE-NP$^{+/-}$ TAMs ($n = 6$ mice). (**D**) Representative IF staining of a PDG-Ink4a/Arf KO glioma showing DAPI$^+$ cell nuclei (blue), CD68$^+$ TAMs (white), IDH2$^+$ cells (red), and CD31$^+$ endothelial cells (yellow). The green arrowheads on the magnification (right) indicate CD68$^+$ IDH2$^+$ cells. Scale bar, 50 µm. (**E**) IF-based Visiopharm quantification of the distance to the vessels (CD31$^+$) of CD68$^+$ IDH2$^+$ and CD68$^+$ IDH2$^-$ TAMs ($n = 6$ mice); *$P < 0.05$, as determined by a paired Wilcoxon test.

^{19}F signal volume at different time points after RT (Fig. 6, A and B). At recurrence, we observed that the ^{19}F signal volume remained constant (Fig. 6A), in contrast to the ^{1}H MRI signal increase that reflected the growth of recurrent tumors (Fig. 5B). Topographical examination of the 19F signal showed that it was restricted to a specific region of the recurrent glioma, which could potentially reflect spatially distinct TAM clusters at recurrence (Fig. 6B). We therefore analyzed the composition of the major TAM populations in untreated and RT-recurrent PDG-Ink4a/Arf KO gliomas in Cx3cr1:CreERT2-IRES-YFP;Rosa26:lslTdTomato mice that allow one to distinguish MG [yellow fluorescent protein–positive (YFP$^+$)/tdTomato$^+$] and MDMs (YFP$^+$/tdTomato$^-$) (termed

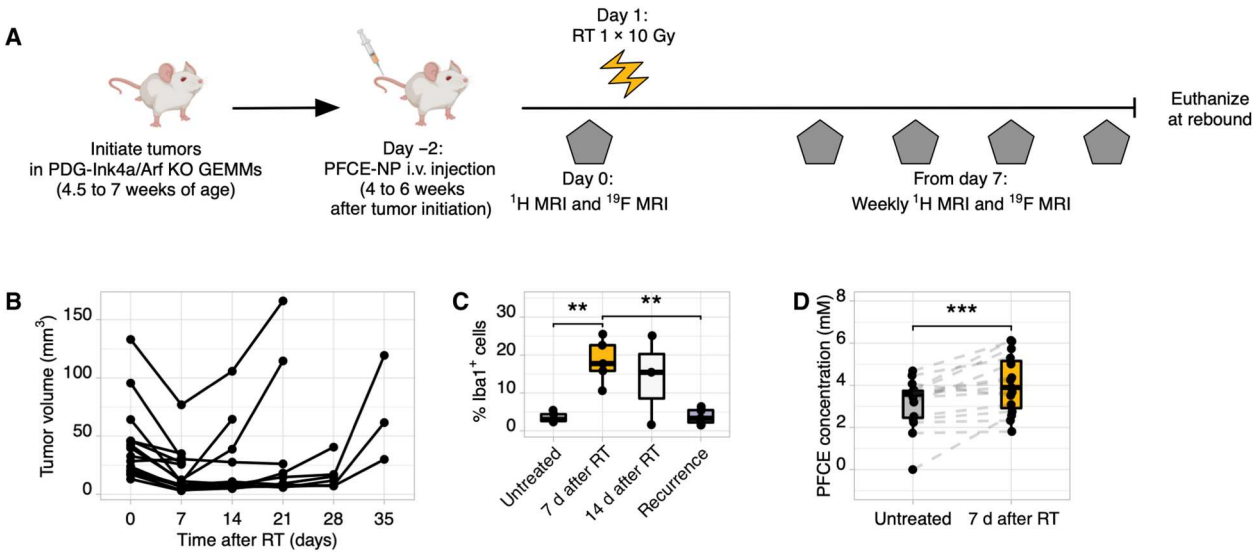

Fig. 5. The increase in TAMs after RT can be longitudinally monitored by ^{19}F MRI. (**A**) Experimental design to monitor TAM dynamics after RT by ^{19}F MRI. At tumor detection, PDG-Ink4a/Arf KO glioma-bearing mice were injected with PFCE-NP and imaged with both conventional ^{1}H and ^{19}F MRI to monitor tumor volume and assess the baseline ^{19}F signal. After the first ^{19}F MRI session, mice were irradiated with a single dose of 10 Gy and then imaged weekly by ^{1}H and ^{19}F MRI until tumor recurrence. (**B**) ^{1}H MRI tumor growth curves in PDG-Ink4a/Arf KO glioma-bearing mice treated with 10 Gy RT (n = 15 mice). (**C**) IF quantification of TAMs using the pan-macrophage marker Iba1, in tissue sections from untreated mice (n = 5), mice at 7 days (n = 5) or 14 days after RT (n = 3), and mice with recurrent (n = 7 mice) PDG-Ink4a/Arf KO gliomas. **P < 0.01, as measured by a post hoc Tukey's multiple comparisons test. (**D**) Quantification of the tumor PFCE concentration before and 7 days after RT (n = 15). ***P < 0.001, as determined by a paired Wilcoxon test.

CX3CR1 lineage tracing model) (*29*, *43*) and by IF staining of the pan-macrophage marker Iba1 and the MG-specific marker P2RY12 (Fig. 6C and fig. S6A). We observed a shift in these TAM populations between untreated and RT-recurrent tumors, consistent with previous flow cytometry findings (*5*). Whereas MG are the predominant TAM population in untreated gliomas, at recurrence, the tumor is abundantly infiltrated by peripheral MDMs, which are unlikely to be detected by ^{19}F MRI based on the lack of peripheral cell labeling by PFCE-NP at this late stage (fig. S2F). Hence, we reasoned that an initial PFCE-NP^{+} TAM population (likely MG predominantly) remains in the residual tumor bed after RT treatment and forms a discrete TAM cluster, whereas the recurrent outgrowing glioma is infiltrated by new (PFCE-NP-unlabeled) myeloid cells originating from the periphery.

Therefore, to capture the integrated cellular, temporal, and spatial complexity of TAM dynamics until recurrence, we decided to investigate the potential use of multispectral ^{19}F MRI, allowing the detection of temporally distinct cell populations (*44*, *45*). Glioma-bearing mice were injected with a single administration of PFCE-NP before RT (single dose of 10 Gy) and monitored by conventional ^{1}H MRI until glioma recurrence. At recurrence, these mice were injected with a second, distinct PFC-NP (PFTBH-NP), which emits a fluorine resonance peak at a separate frequency from PFCE, and a final ^{1}H and ^{19}F MRI was performed (Fig. 6D and fig. S6B) (*23*). We found that the ^{19}F signal from PFTBH-NP mainly covered a region of the tumor that did not show signal from the original PFCE-NP (Fig. 6, E and F). Moreover, the cumulative ^{19}F signal volume was significantly higher than the original PFCE-NP ^{19}F signal volume alone (P < 0.01; Fig. 6G), showing a volumetric dynamic that was similar to conventional ^{1}H MRI monitoring, where larger tumor volumes were detected at recurrence (Fig. 5B). Whereas the ^{19}F SNR of the PFCE and PFTBH compounds was similar in the liver, it was higher for PFCE in the tumor, possibly as a consequence of the initial PFCE concentration increase after RT (fig. S6, C and D). Accordingly, we inferred that TAMs not only shift their relative proportion between MG and MDMs after RT but that this multispectral ^{19}F MRI strategy could reveal alterations in their spatial organization that potentially differ in untreated and recurrent gliomas, which we therefore investigated further.

The distribution pattern of TAMs within tumors changes after RT treatment

We explored how the spatial and temporal distribution of TAMs changes after RT treatment by analysis of tissue sections. IF staining of PDG-Ink4a/Arf KO gliomas in the CX3CR1 lineage tracing background showed differences in the spatial distribution of TAMs between untreated and recurrent tumors, where substantial MDM-rich areas could be observed specifically at recurrence (Fig. 7A). To quantify this observation, we analyzed the average distance between MDMs and MG (Fig. 7B) and found that MDMs were significantly more distant from MG in recurrent tumors compared to untreated gliomas, indicative of this clustering phenomenon (P < 0.05). To assess a potential spatial mutual exclusion between the two cell types, we analyzed the frequency of MG in a region of interest defined around MDMs (termed MDM-ROI) in untreated and recurrent tumors (Fig. 7C). We found a significantly lower abundance of MG in MDM-rich areas at recurrence (P < 0.05; Fig. 7D). Collectively, these results showed that, although MDMs and MG are generally evenly distributed within untreated tumors, at recurrence, we observe the spatial emergence of localized clusters

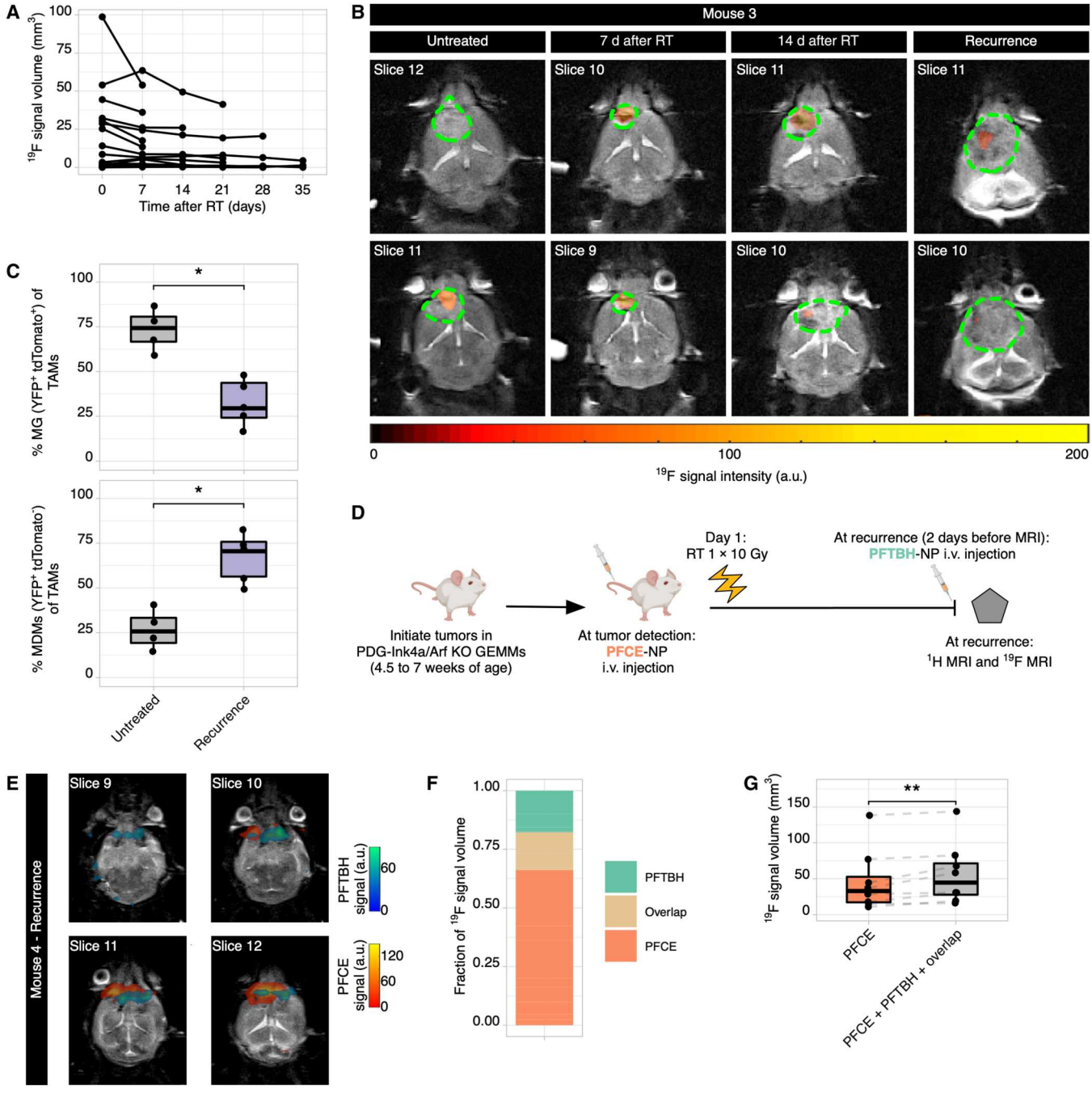

Fig. 6. Multispectral ^{19}F MRI identifies temporally distinct niches in recurrent gliomas. (**A**) Tumor ^{19}F signal volume curves in PDG-Ink4a/Arf KO glioma-bearing mice treated with 10 Gy RT ($n = 15$ mice). (**B**) Representative ^{19}F and ^{1}H MRI overlay images of the same mouse showing the tumor (green dashed line) and the PFCE ^{19}F signal (orange mask) over the full length of the RT trial. (**C**) IF-based quantification of MG (top) and MDMs (bottom) in untreated and recurrent glioma tissue sections. To identify MG and MDMs, respectively, we used Cx3cr1:CreERT2-IRES-YFP;Rosa26:lslTdTomato mice that express tdTomato in *Cx3cr1*-expressing cells (MG and circulating blood monocytes) upon tamoxifen injection. Three weeks after tamoxifen-induced labeling, when blood monocytes are replenished by tdTomato$^-$ cells and only MG remain tdTomato$^+$, PDG-Ink4a/Arf KO gliomas were induced. (**D**) Experimental design to monitor TAM temporal dynamics after RT by multispectral ^{19}F MRI. Glioma-bearing mice were injected with PFCE-NP before RT and monitored weekly with conventional ^{1}H MRI. At detection of recurrence, mice were injected with PFTBH-NP and imaged 2 days later with ^{1}H and ^{19}F MRI, sequentially acquiring both PFCE and PFTBH signals. (**E**) ^{1}H and ^{19}F MRI overlay images of the same animal showing the distinct PFCE ^{19}F signal (red to yellow mask) and the PFTBH ^{19}F signal (blue to green mask). (**F**) Quantification of the individual compound volume fraction from the total ^{19}F signal volumes. (**G**) Quantification of the ^{19}F signal volume of PFCE only and the cumulative ^{19}F volume, respectively. *$P < 0.05$ and **$P < 0.01$, as determined by unpaired Mann-Whitney test in (C) and paired Wilcoxon test in (G).

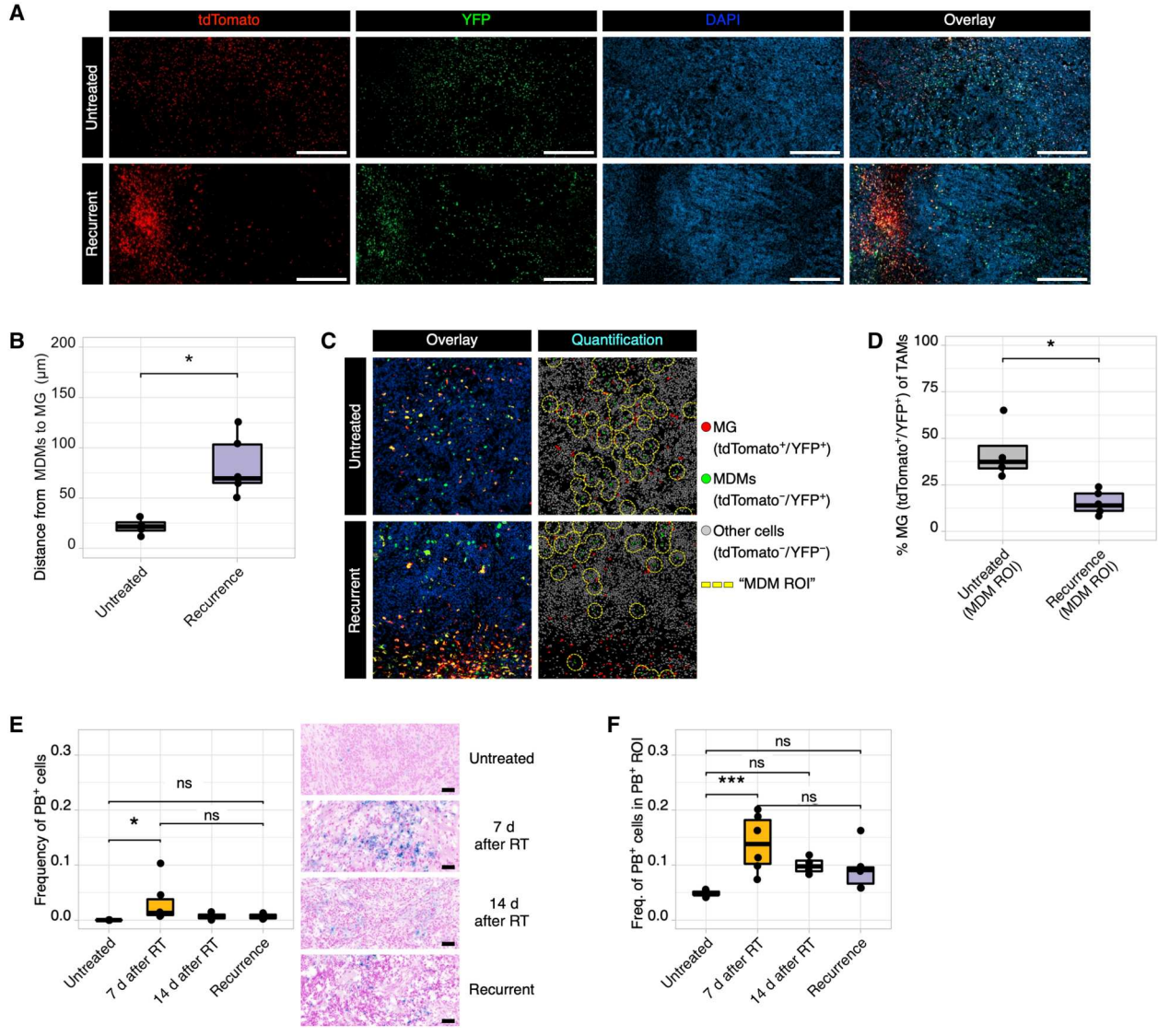

Fig. 7. MG and MDMs are differentially distributed in untreated and recurrent gliomas. (**A**) Representative IF images of the MG-specific tdTomato expression and pan-TAM YFP expression in untreated (top) and RT recurrent (bottom) PGD-Ink4a/Arf KO gliomas in the CX3CR1 lineage tracing model. Scale bars, 500 μm. (**B**) IF-based quantification of the average distance of YFP$^+$/tdTomato$^-$ MDMs to YFP$^+$/tdTomato$^+$ MG. (**C**) Visiopharm quantification pipeline showing YFP$^+$/tdTomato$^+$ MG (red), YFP$^+$/tdTomato$^-$ MDMs (green), and other non-TAM YFP$^-$/tdTomato$^-$ cells. The yellow dashed line outlines the "MDM ROI" defined around each MDM nucleus. (**D**) IF quantification of YFP$^+$/tdTomato$^+$ MG in the MDM ROI in untreated and RT-recurrent tumors. (**E**) Prussian blue (PB) staining quantification of PB$^+$ cells in tumor tissues at different time points before and after RT; corresponding representative images are shown on the right. (**F**) Frequency of PB$^+$ cells per PB ROI in the different treatment groups. Scale bars, 50 μm. *P < 0.05, unpaired Mann-Whitney test (B and D). *P < 0.05, ***P < 0.001, not significant if not otherwise stated, post hoc Tukey's multiple comparisons test (E and F).

of distinct TAM populations, as initially indicated by the ^{19}F MRI analyses.

Although these analyses revealed different spatial patterns of TAMs in untreated versus RT-recurrent tumors, it did not enable the temporal discrimination of the sequence of cell infiltration throughout the experimental time course. Given that RT has been reported to lead to hemolysis and hemoglobin release in other contexts (*46*, *47*), we assessed whether this process is also evident in gliomas after RT and whether iron uptake by specific cells could thereby mark them in a temporal manner. We therefore stained PDG-Ink4a/Arf KO glioma sections with Prussian blue (PB) to visualize iron deposition. Although there were only rare PB$^+$ cells in untreated tumors, we found a peak of PB$^+$ cells at 7 days after RT (Fig. 7E). To identify the cellular source of the PB signal, we multiplexed PB and IF staining (fig. S7A) and found MDMs to be the main cell type accumulating iron, whereas no PB$^+$ MG were observed (fig. S7B). To confirm these findings, we analyzed a published gene expression dataset of MG and MDMs in untreated, 5 day–irradiated and RT-recurrent gliomas (*5*). GSEA indeed showed increased iron uptake–related processes at 5 days after RT and at recurrence specifically in MDMs but not in MG, thus supporting our observation of an increased frequency of PB$^+$ cells after

RT treatment (fig. S7C). Together, these results revealed the emergence of a temporally defined PB^+ population (mainly MDMs) only after RT.

Last, we investigated whether the PB^+ cells remained in proximity to one another in recurrent gliomas. We analyzed their frequency in the whole tumor area and in a defined ROI around PB^+ cells (termed PB^+ ROI) (fig. S7D). We found that the frequency of PB^+ cells in the PB^+ ROI was higher in recurrent than untreated tumors (Fig. 7F). This indicates that these cells cluster together during tumor outgrowth and form a spatially defined niche, despite their generally low abundance overall (Fig. 7E). In sum, through these analyses, we found that, in recurrent tumors, there was a higher infiltration of MDMs, which localize distally from MG. PB^+ cells, which were mainly MDMs, were enriched after RT treatment and also cluster together in the larger recurrent tumors. These results show that different TAM populations, in addition to shifting their relative abundance in a dynamic manner, can also vary in spatial distribution in a time-dependent manner, as revealed by our multispectral ^{19}F MRI strategy (fig. S8).

DISCUSSION

MRI is indispensable in neuro-oncology practice, yet quantitative, standardized, and robust MRI-based biomarkers are currently sparse (*16*). Recent clinical studies demonstrated the potential of MRI in predicting the response to antiangiogenic treatment in pediatric and adult brain tumors (*48*, *49*). Quantitative characterization of vascular properties is a common MRI application in the imaging of brain tumors, due to the ability of gadolinium-based contrast agents to penetrate and enhance those tumor regions with a disrupted BBB (*50*, *51*). Nonetheless, the vasculature is just one component of the complex brain TME (*1*). Despite the high abundance of TAMs in gliomas (*3*, *4*) and their importance in establishing an immunosuppressive TME (*52*) with potential direct consequences on the effectiveness of immunotherapeutic strategies in patients (*53*), TAM abundance and distribution can currently only be assessed after an invasive surgical procedure to remove tumor tissue.

In this study, we harnessed the power of ^{19}F multispectral MRI in preclinical glioma and brain metastasis models to show the technological feasibility of longitudinally and noninvasively imaging small inflamed brain tumors in vivo with a clinical scanner at high spatial resolution. These results highlight the translational potential of this strategy to expand the MRI repertoire used to classify diverse brain malignancies (*54*). We found substantial differences in the ^{19}F signal distribution between the preclinical glioma and brain metastasis models, underlining a potential relevance for distinguishing these two brain tumor types. This result is supported by the lower overall TAM abundance observed in both preclinical BrM models and patient BrM tissues compared to gliomas (*3*, *4*, *55*), which can thus explain the observed lower accumulation of PFCE-NP in the BrM model. Moreover, the presence of the BBB plays a crucial role in regulating the delivery of the PFCE-NP, which was more efficient in the primary breast tumor setting compared to the breast-BrM model.

To date, the application of PFCs to image immune cells in cancer has largely relied on the ex vivo labeling of specific cell types in the context of monitoring cell-based therapies, such as adoptive T cell transfer and dendritic cell–based cancer vaccination (*56*, *57*). In vivo, only a handful of studies have explored the distribution of injected PFC-NP to image myeloid cells (*25*, *34*, *37*, *58*–*60*), and the subcellular composition of the labeled myeloid cells has been minimally investigated (*61*). Moreover, the extent of brain microenvironmental heterogeneity has been underscored by recent single-cell analyses, with potential translational implications (*62*). In this study, we found that PFCE-NP in preclinical glioma models label several myeloid cell subpopulations, mostly comprising resident MG and peripheral MDMs, which also displayed heterogeneity and likely contain additional cell subpopulations. Both MG and MDMs were labeled directly within the tumor and were not evidently replenished by newly infiltrating immune cells in the weeks after PFCE-NP administration. Moreover, our gene expression analysis revealed rhodamine-PFCE-NP^+ TAMs to be characterized by specific metabolic signatures, which may relate to critical phenotypes and functions (*42*, *63*, *64*), and was associated with their enrichment in the perivascular niche. It will be important to perform additional characterization of the TAM subsets that uptake PFCE-NP, for example, using single-cell analysis, and explore the role of additional macrophage populations, including central nervous system (CNS) border–associated macrophages (*65*).

Our data also showed that TAMs are the predominant, although not the sole cell population taking up PFCE-NP. Nonimmune cells were the second largest PFCE-NP^+ population, including endothelial cells, thereby indicating an active role of the vasculature in the trafficking of these NP in vivo. Uptake in other nonimmune cells included a small proportion of cancer cells and potentially other nonimmune nonmalignant cell types. Rapidly dividing cells have been shown to actively engulf NP by macropinocytosis (*66*, *67*). Moreover, brain-resident astrocytes also have phagocytic ability (*68*). Thus, future studies will be important to further explore the precise ontogeny of the rare nonimmune cell types incorporating NP, as well as the underlying cellular mechanism for NP uptake. Although several studies have demonstrated a clear role for phagocytosis and macropinocytosis in PFC-NP uptake in vitro (*26*, *27*), further research is required to better understand this process in vivo. Hence, the IVM method presented in this study might be a valuable approach to address these open questions and aid in designing cell type–specific NP to selectively label and target only the population of interest.

TAM content and composition are in constant flux and adaptation during tumor growth and in response to therapies (*5*, *8*). In this context, ^{19}F MRI represents a powerful strategy to temporally and spatially track distinct inflammatory dynamics in RT-recurrent tumors by performing multispectral imaging using PFCE-NP and PFTBH-NP. This allowed us to gain new insights into the presence of different TME niches not only before treatment and at recurrence but also during tumor dormancy, when the tumor had regressed and tumor volume was stable. Emergence of therapy resistance from a dormant state is known to be a key step involving TAM-mediated mechanisms in response to different therapeutic interventions (*5*, *11*), although a noninvasive clinical assessment of TAMs in dormant tumors has not been achievable to date. Our analyses revealed that gliomas not only shift the ratio of MDM to MG in response to RT but also differ in the spatial distribution of these distinct cell populations. This finding has relevance for understanding the complexity of the brain TME by integrating temporal and spatial parameters. In this context, it will be important to assess whether these TAM-defined microenvironmental niches respond differently

to specific treatments, for example. Moreover, we also identified an RT-triggered iron-rich TAM population that occupied a specific niche from 7 days after RT through to tumor recurrence. Iron is an essential metal micronutrient, and its metabolism in tumors is regulated by TAMs, with a direct impact on tumor growth and on the immune response of macrophages themselves (*69*), suggesting that this specific cell population may play an important role in adaptive resistance.

NP-based drug delivery and anti-angiogenic treatments have been widely studied in brain tumors with several objectives and potential applications. The first is to improve the delivery of compounds with a poor pharmacokinetic profile, leading to optimal drug release and potentially reducing drug side effects (*70*). The second is to normalize the vasculature, thereby resulting in improved drug delivery (*39*). The unique structure of the BBB, however, requires a careful and meticulous investigation of the effect of vascular integrity on drug delivery (*39*). Vessel normalization has been shown to enhance the efficacy of chemotherapeutic agents in preclinical glioma models (*71*). However, a study of multiple pediatric brain tumor models, driven by distinct oncogenic alterations, revealed a differential impairment of the BBB, which resulted in effective chemotherapy delivery only in medulloblastoma with disrupted vessels (*72*). Our findings in this study directly connect the heterogeneity of the vasculature with the extent of PFCE-NP accumulation. The NP only accumulated in areas of dysmorphic vessels, highlighting the notion that vessel normalization in brain tumors needs to take into consideration the type and size of any additional combinatorial drug treatments. ^{19}F MRI can thus represent a potential MRI-based method to gain important information regarding the extent and heterogeneity of BBB leakage, which is conventionally assessed using gadolinium-based contrast agents at present, and could be linked to the abundance, phenotype, and cellular identity of TAMs.

In this study, we characterized the TAM subpopulation accumulating the NP in considerable depth. Nonetheless, there are some limitations and areas for future investigation, including identifying the mechanism for NP uptake and determining how this might be affected by specific pro-tumorigenic or anti-tumorigenic TAM phenotypes, such as differential phagocytic behavior. This could also be critical for any clinical application of this imaging technique to different tumor types, where TAMs are known to play multifaceted biological roles. Moreover, RT has been shown to phenotypically modulate these cells (*5*). Therefore, future studies will be important to determine whether there is differential uptake of the PFCE- and PFTBH-NP depending on the RT treatment course.

In conclusion, we propose multispectral ^{19}F MRI as a powerful strategy to noninvasively and longitudinally explore brain TME composition and functionality. In the future, it will be of interest to assess its diagnostic and prognostic impact for brain malignancy–related processes, including pseudo-progression, pseudo-regression, and necrotic inflammation to inform the clinical management of the disease. Future studies will also test the ability of multispectral ^{19}F MRI to predict therapy response to targeted treatments, including in other CNS diseases.

MATERIALS AND METHODS

Study design

The aim of this study was to longitudinally and noninvasively monitor TAM dynamics with multispectral ^{19}F MRI over the course of tumor response to RT. The sample size for longitudinal imaging trials (n = 8 to 15 mice) was based on previous experience using these glioma models (*5*, *10*, *11*, *29*) and planned using the statistical program OpenEpi (*73*). ^{19}F signal monitoring was the primary outcome of these experiments. These data were supported by tissue staining, flow cytometry, ex vivo and in vivo imaging, and RNA-seq to further understand the kinetics and distribution of the NP and the underlying biological mechanisms of the MRI-based observations. The choice of defined individual time points for these analyses was based on previously published data on NP kinetics (*22*, *40*), and sample size (n = 3 to 8) was defined as described above. Age-matched mice were assigned to experimental cohorts based on matching tumor volumes, and data presented include all outliers. Investigators were not blinded when treating and monitoring the animals. Blinding was applied during all data analysis. Biological replicates are indicated in the figure legends by n, together with the statistical analysis applied. Two or more independent trials or experiments were performed for all preclinical models, with the exception of the primary breast cancer model, which was performed in a single experimental cohort. All animal studies were reviewed and approved by the Institutional Animal Care and Use Committees of the University of Lausanne and Canton Vaud, Switzerland.

Animals

The Nestin-Tv-a;*Ink4a/Arf*$^{-/-}$ mouse line has been previously described (*74*) and was provided by E. Holland, USA. *Cx3cr1*:CreER-IRES-YFP mice (C57BL/6J background; The Jackson Laboratory) were crossed with Rosa26:lsl-TdTomato reporter mice (C57BL/6J background; The Jackson Laboratory) and with Nestin-Tv-a;*Ink4a/Arf*$^{-/-}$mice (*29*). For the Cx3cr1:CreER-IRES-YFP Rosa26:lsl-TdTomato lineage tracing system, 3- to 4 week-old mice were injected twice, 48 hours apart, intraperitoneally with 1 mg of tamoxifen citrate (Sigma-Aldrich) dissolved in sunflower seed oil (Sigma-Aldrich). Mice were used for intracranial injection surgery 3 weeks after tamoxifen administration (see the "Glioma model" section below). Wild-type female C57BL/6J mice were used for the PyMT-BrM3 brain metastasis (BrM) and primary breast tumor models. All mice were bred within the University of Lausanne animal facilities, and all animal studies were first approved by the Institutional Animal Care and Use Committees of the University of Lausanne and Canton Vaud, Switzerland.

Glioma model

Mice (4.5 to 7 weeks old) were intracranially injected as previously described (*10*, *11*, *28*, *29*). Briefly, mice were fully anesthetized using isoflurane inhalation anesthesia (2% isoflurane/O_2 mixture). A mixture of 2% lidocaine (Streuli Pharma) and 0.5% bupivacaine (Carbostesin, Aspen Pharma Schweiz) was applied as a local analgesic (50 μl per mouse), and buprenorphine (0.3 mg/ml; Temgesic, Indivior Schweiz) was given subcutaneously as a systemic analgesic (100 μl per mouse). Using a stereotactic apparatus, cells were injected into the right frontal cortex (2 mm frontal, 1.5 mm lateral from bregma, 2 mm deep). Mice were injected with 2×10^5 RCAS-PDGFB-HA or PDGFB-HA-SV40-GFP DF1 cells. The skin incision

was sealed with Vetbond tissue adhesive (3M), and the mouse was placed on a heating pad and monitored until fully recovered from anesthesia. Last, Bepanthen cream (Bayer) was applied on the incision site before placing the animal back in the cage, and each mouse was followed by regular monitoring.

Generation of experimental brain metastasis

The initiation of brain metastasis from the PyMT-BrM3 line was performed as previously described for other BrM derivatives (*29*, *75*, *76*). Briefly, PyMT-BrM3 cells were resuspended in Hanks' balanced salt solution (Life Technologies), and 1×10^5 cells were inoculated into the left cardiac ventricle of 6- to 10-week-old female C57BL/6J mice.

Generation of experimental primary breast tumor model

For the generation of primary breast tumors, 6- to 10-week-old female C57BL/6J mice were anesthetized using isoflurane inhalation. PyMT-BrM3 cells (7×10^5) resuspended in 50% Matrigel (catalog no. 356231, Corning) were injected orthotopically in the mammary fat pad. Mice were regularly monitored, and tumor volumes were assessed twice per week using calipers. Tumor volumes were calculated as vol = (width^2 × length).

Perfluorocarbon treatment

An initial PFC emulsion based on 10% (w/v) PFCE was prepared in-house as described previously [20% (w/v) emulsions were used for experiments with the primary breast tumor model] (*22*, *40*). The emulsion contains NP with a mean size of 200 nm and produces a single spectral line at −92.8 parts per million (ppm). A second, similar PFCE emulsion was prepared with rhodamine to enable fluorescence-activated cell sorting. A third PFC emulsion based on 60% (w/v) PFTBH (*23*) was provided by Aurum Biosciences. PFTBH produces a singlet spectral line at −61.5 ppm (a 3650-Hz shift from PFCE) that is used for imaging and a multiplet that ranges from −115 to −144 ppm (*23*).

^{1}H and ^{19}F MR imaging acquisition

All MRI experiments were performed on a 3T clinical system (MAGNETOM Prisma, Siemens Healthineers). A 35-mm-diameter transmit/receive birdcage radiofrequency coil, tunable to both the ^{19}F and ^{1}H frequencies (Rapid Biomedical), was used for both excitation and signal detection. Two days after the PFC-NP injection, the animals were anesthetized with 2.5% isoflurane in oxygen for 1 to 2 min. Anesthesia was maintained with 1.5 to 2% of isoflurane for the duration of the scan. The body temperature was monitored with a rectal probe and maintained at 37.0° ± 0.5°C with a tubing system circulating warm water, and the respiratory activity was monitored by means of a respiration pillow placed below the mouse abdomen (all SA Instruments). An external reference tube with a known concentration of PFCE-NP (18.95 mM) in 2% (w/v) agar gel (Life Technologies) was created and used for absolute quantification. The tube was carefully placed diagonally below and to the side of the brain of the animal (below the shoulders) such that any artifactual signal emitted from this reference did not interfere with the signal from the brain. In the dual-PFC experiments, a second probe with PFTBH-NP (40 mM) was placed adjacent to the other shoulder of the animal. Multiplanar low-resolution scout scans were then performed for anatomic localization. For glioma and primary breast tumor model imaging, a high-resolution T_2-weighted 3D turbo spin echo (TSE) scan was acquired in an axial orientation. The following pulse sequence parameters were used: repetition time (TR) = 4500 ms; echo time (TE) = 80 ms; echo train length (ETL) = 32; pixel bandwidth (BW) = 130 Hz/pixel; field of view (FOV) = 60 mm × 60 mm × 32 mm; voxel size = 0.16 mm × 0.16 mm × 1 mm; number of slices = 32; slice oversampling = 12.5%; and acquisition time (T_{acq}) = 32 min and 19 s. For metastasis imaging, mice were injected intraperitoneally with 150 μl Gadobutrol (Gadovist, 1 mmol/ml; Bayer) 10 min before the measurement. A high-resolution T_1-weighted 3D gradient–recalled echo scan was acquired with the following parameters: TR = 280 ms; TE = 3.4 ms; BW = 320 Hz/pixel; FOV = 60 mm × 60 mm × 20 mm; voxel size = 0.21 mm × 0.21 mm × 1 mm; number of slices = 20; slice oversampling = 10%; and T_{acq} = 29 min and 33 s. ^{19}F MR images of PFCE were obtained using a 3D TSE pulse sequence with the following sequence parameters optimized for maximal SNR in 30 min (*77*): TR = 2460 ms; TE = 13 ms; BW = 130 Hz/pixel; ETL = 43; FOV = 100 mm × 100 mm × 16 mm; voxel size = 0.78 mm × 0.78 mm × 1 mm; number of slices = 16; slice oversampling = 12.5%; number of signal averages (NA) = 14; and T_{acq} = 30 min and 57 s. The center of the 3D volume was placed at the same position as the ^{1}H 3D volume. When PFTBH was imaged, the ^{19}F resonance frequency was shifted to the appropriate frequency, and the same 3D TSE pulse sequence was used but with TR = 2850 ms, NA = 9, ETL = 35, and T_{acq} = 30 min and 44 s.

MR image analysis

^{1}H images produced by the MR scanner in dicom format were copied, and the ^{19}F images were reconstructed from raw data in MATLAB (MathWorks) to ensure that the background noise was correctly digitized. All subsequent image analyses were then performed in MATLAB. The ^{1}H and ^{19}F MR images were postprocessed in several semi-automated steps to obtain reproducible and consistent PFC quantifications. The tumor outline was manually delineated in the high-resolution ^{1}H images to calculate the ^{1}H tumor volume. The slice numbers that visually contained tumor tissue were retained to constrain the ^{19}F calculations. In the stack of ^{19}F images, a rectangular ROI was drawn at the edge of the image (where no tissue was present) to determine the amount of background noise for subsequent thresholding. The ^{19}F images were then flattened into a maximum intensity projection (MIP) on which broad ROIs were drawn around the tumor, reference tube, and liver. These MIP ROIs were then copied to all slices. Simultaneously, the ^{19}F images were automatically thresholded at 6× the SD of the previously determined background noise threshold to generate a mask that satisfies the Rose criterion (*78*), avoids the inclusion of low-amplitude ghosting artifacts, and thus only contains voxels with a high ^{19}F signal. To reproducibly generate an ROI that only included the voxels with signal from the tumor, the retained ^{1}H slices, the manually drawn ^{19}F MIP ROI, and the ^{19}F threshold mask were multiplied. This procedure was then repeated to generate selective liver and reference tube ROIs. The average ^{19}F signal in these ROIs was divided by the ^{19}F noise SD described above to calculate the tumor, liver, and reference tube ^{19}F SNR. The ^{19}F signal, SNR, and ROI volume of each animal were retained and used together with the known reference tube concentration to calculate the tumor and liver PFC concentration. This was performed as follows: The average ^{19}F signal in the tumor or liver ROI was divided by the average ^{19}F signal in the reference tube ROI and

was multiplied by the known reference tube concentration. Total amounts of tumor PFC were calculated by multiplying the PFC concentration with the PFC signal volume.

Statistical analysis

All raw, individual-level data for experiments where $n < 20$ are included in data file S1. R version 4.1.0 was used to perform statistical analysis and graphically plot all data (ggplot package). Parametric data were analyzed by a two-tailed Student's t test (paired or unpaired depending on the experimental setup). Nonparametric data were analyzed by a Mann-Whitney test on ranks (paired or unpaired depending on the experimental setup). $P < 0.05$ was considered as statistically significant. Each specific statistical test is reported for each experiment in the figure legends. Boxplots are used to present the data, showing median and the 25th to 75th percentiles.

Supplementary Materials

This PDF file includes:
Materials and Methods
Figs. S1 to S8
Table S1

Other Supplementary Material for this manuscript includes the following:
Movies S1 to S3
Data file S1
MDAR Reproducibility Checklist

View/request a protocol for this paper from *Bio-protocol*.

REFERENCES AND NOTES

1. D. F. Quail, J. A. Joyce, The microenvironmental landscape of brain tumors. *Cancer Cell* **31**, 326–341 (2017).
2. B. M. Andersen, C. Faust Akl, M. A. Wheeler, E. A. Chiocca, D. A. Reardon, F. J. Quintana, Glial and myeloid heterogeneity in the brain tumour microenvironment. *Nat. Rev. Cancer* **21**, 786–802 (2021).
3. F. Klemm, R. R. Maas, R. L. Bowman, M. Kornete, K. Soukup, S. Nassiri, J. P. Brouland, C. A. Iacobuzio-Donahue, C. Brennan, V. Tabar, P. H. Gutin, R. T. Daniel, M. E. Hegi, J. A. Joyce, Interrogation of the microenvironmental landscape in brain tumors reveals disease-specific alterations of immune cells. *Cell* **181**, 1643–1660.e17 (2020).
4. E. Friebel, K. Kapolou, S. Unger, N. G. Nunez, S. Utz, E. J. Rushing, L. Regli, M. Weller, M. Greter, S. Tugues, M. C. Neidert, B. Becher, Single-cell mapping of human brain cancer reveals tumor-specific instruction of tissue-invading leukocytes. *Cell* **181**, 1626–1642.e20 (2020).
5. L. Akkari, R. L. Bowman, J. Tessier, F. Klemm, S. M. Handgraaf, M. de Groot, D. F. Quail, L. Tillard, J. Gadiot, J. T. Huse, D. Brandsma, J. Westerga, C. Watts, J. A. Joyce, Dynamic changes in glioma macrophage populations after radiotherapy reveal CSF-1R inhibition as a strategy to overcome resistance. *Sci. Transl. Med.* **12**, eaaw7843 (2020).
6. D. N. Louis, A. Perry, P. Wesseling, D. J. Brat, I. A. Cree, D. Figarella-Branger, C. Hawkins, H. K. Ng, S. M. Pfister, G. Reifenberger, R. Soffietti, A. von Deimling, D. W. Ellison, The 2021 WHO classification of tumors of the central nervous system: A summary. *Neuro Oncol.* **23**, 1231–1251 (2021).
7. R. Stupp, W. P. Mason, M. J. van den Bent, M. Weller, B. Fisher, M. J. Taphoorn, K. Belanger, A. A. Brandes, C. Marosi, U. Bogdahn, J. Curschmann, R. C. Janzer, S. K. Ludwin, T. Gorlia, A. Allgeier, D. Lacombe, J. G. Cairncross, E. Eisenhauer, R. O. Mirimanoff; European Organisation for Research and Treatment of Cancer Brain Tumor and Radiotherapy Groups; National Cancer Institute of Canada Clinical Trials Group, Radiotherapy plus concomitant and adjuvant temozolomide for glioblastoma. *N. Engl. J. Med.* **352**, 987–996 (2005).
8. P. Magod, I. Mastandrea, L. Rousso-Noori, L. Agemy, G. Shapira, N. Shomron, D. Friedmann-Morvinski, Exploring the longitudinal glioma microenvironment landscape uncovers reprogrammed pro-tumorigenic neutrophils in the bone marrow. *Cell Rep.* **36**, 109480 (2021).
9. J. Kowal, M. Kornete, J. A. Joyce, Re-education of macrophages as a therapeutic strategy in cancer. *Immunotherapy* **11**, 677–689 (2019).
10. S. M. Pyonteck, L. Akkari, A. J. Schuhmacher, R. L. Bowman, L. Sevenich, D. F. Quail, O. C. Olson, M. L. Quick, J. T. Huse, V. Teijeiro, M. Setty, C. S. Leslie, Y. Oei, A. Pedraza, J. Zhang, C. W. Brennan, J. C. Sutton, E. C. Holland, D. Daniel, J. A. Joyce, CSF-1R inhibition alters macrophage polarization and blocks glioma progression. *Nat. Med.* **19**, 1264–1272 (2013).
11. D. F. Quail, R. L. Bowman, L. Akkari, M. L. Quick, A. J. Schuhmacher, J. T. Huse, E. C. Holland, J. C. Sutton, J. A. Joyce, The tumor microenvironment underlies acquired resistance to CSF-1R inhibition in gliomas. *Science* **352**, aad3018 (2016).
12. D. Yan, J. Kowal, L. Akkari, A. J. Schuhmacher, J. T. Huse, B. L. West, J. A. Joyce, Inhibition of colony stimulating factor-1 receptor abrogates microenvironment-mediated therapeutic resistance in gliomas. *Oncogene* **36**, 6049–6058 (2017).
13. I. L. Tan, R. D. N. Arifa, H. Rallapalli, V. Kana, Z. Lao, R. M. Sanghrajka, N. Sumru Bayin, A. Tanne, A. Wojcinski, A. Korshunov, N. Bhardwaj, M. Merad, D. H. Turnbull, J. J. Lafaille, A. L. Joyner, CSF1R inhibition depletes tumor-associated macrophages and attenuates tumor progression in a mouse sonic Hedgehog-Medulloblastoma model. *Oncogene* **40**, 396–407 (2021).
14. F. Klemm, A. Mockl, A. Salamero-Boix, T. Alekseeva, A. Schaffer, M. Schulz, K. Niesel, R. R. Maas, M. Groth, B. T. Elie, R. L. Bowman, M. E. Hegi, R. T. Daniel, P. S. Zeiner, J. Zinke, P. N. Harter, K. H. Plate, J. A. Joyce, L. Sevenich, Compensatory CSF2-driven macrophage activation promotes adaptive resistance to CSF1R inhibition in breast-to-brain metastasis. *Nat. Cancer* **2**, 1086–1101 (2021).
15. M. G.-M. C. Lin, T. M. Bauer, A. Naing, D. Wan-Teck Lim, J. Sarantopoulos, R. Geva, Y. Ando, L. Fan, S. Choudhury, P. Tu, C. Quadt, A. Santoro, Phase I study of BLZ945 alone and with spartalizumab (PDR001) in patients (pts) with advanced solid tumors [abstract]. *Cancer Res.* **80**, CT171 (2020).
16. M. Smits, MRI biomarkers in neuro-oncology. *Nat. Rev. Neurol.* **17**, 486–500 (2021).
17. H. Mehrabian, J. Detsky, H. Soliman, A. Sahgal, G. J. Stanisz, Advanced magnetic resonance imaging techniques in management of brain metastases. *Front. Oncol.* **9**, 440 (2019).
18. Q. Li, F. Dong, B. Jiang, M. Zhang, Exploring MRI characteristics of brain diffuse midline gliomas with the H3 K27M mutation using radiomics. *Front. Oncol.* **11**, 646267 (2021).
19. D. Li, C. B. Patel, G. Xu, A. Iagaru, Z. Zhu, L. Zhang, Z. Cheng, Visualization of diagnostic and therapeutic targets in glioma with molecular imaging. *Front. Immunol.* **11**, 592389 (2020).
20. S. Mukherjee, D. Sonanini, A. Maurer, H. E. Daldrup-Link, The yin and yang of imaging tumor associated macrophages with PET and MRI. *Theranostics* **9**, 7730–7748 (2019).
21. R. Weissleder, M. Nahrendorf, M. J. Pittet, Imaging macrophages with nanoparticles. *Nat. Mater.* **13**, 125–138 (2014).
22. C. Jacoby, S. Temme, F. Mayenfels, N. Benoit, M. P. Krafft, R. Schubert, J. Schrader, U. Flogel, Probing different perfluorocarbons for in vivo inflammation imaging by 19F MRI: Image reconstruction, biological half-lives and sensitivity. *NMR Biomed.* **27**, 261–271 (2014).
23. E. Darcot, R. Colotti, D. Brennan, G. A. Deuchar, C. Santosh, R. B. van Heeswijk, A characterization of ABL-101 as a potential tracer for clinical fluorine-19 MRI. *NMR Biomed.* **33**, e4212 (2020).
24. U. Flögel, Z. Ding, H. Hardung, S. Jander, G. Reichmann, C. Jacoby, R. Schubert, J. Schrader, In vivo monitoring of inflammation after cardiac and cerebral ischemia by fluorine magnetic resonance imaging. *Circulation* **118**, 140–148 (2008).
25. R. B. van Heeswijk, M. Pellegrin, U. Flogel, C. Gonzales, J. F. Aubert, L. Mazzolai, J. Schwitter, M. Stuber, Fluorine MR imaging of inflammation in atherosclerotic plaque in vivo. *Radiology* **275**, 421–429 (2015).
26. F. Nienhaus, D. Colley, A. Jahn, S. Pfeiler, V. Flocke, S. Temme, M. Kelm, N. Gerdes, U. Flogel, F. Bonner, Phagocytosis of a PFOB-nanoemulsion for ^{19}F magnetic resonance imaging: First results in monocytes of patients with stable coronary artery disease and ST-elevation myocardial infarction. *Molecules* **24**, (2019).
27. E. T. Ahrens, R. Flores, H. Xu, P. A. Morel, In vivo imaging platform for tracking immunotherapeutic cells. *Nat. Biotechnol.* **23**, 983–987 (2005).
28. D. Hambardzumyan, N. M. Amankulor, K. Y. Helmy, O. J. Becher, E. C. Holland, Modeling adult gliomas using RCAS/t-va technology. *Transl. Oncol.* **2**, 89–95 (2009).
29. R. L. Bowman, F. Klemm, L. Akkari, S. M. Pyonteck, L. Sevenich, D. F. Quail, S. Dhara, K. Simpson, E. E. Gardner, C. A. Iacobuzio-Donahue, C. W. Brennan, V. Tabar, P. H. Gutin, J. A. Joyce, Macrophage ontogeny underlies differences in tumor-specific education in brain malignancies. *Cell Rep.* **17**, 2445–2459 (2016).
30. C. J. Herting, Z. Chen, V. Maximov, A. Duffy, F. Szulzewsky, D. M. Shayakhmetov, D. Hambardzumyan, Tumour-associated macrophage-derived interleukin-1 mediates glioblastoma-associated cerebral oedema. *Brain* **142**, 3834–3851 (2019).
31. A. Di Costanzo, T. Scarabino, F. Trojsi, T. Popolizio, D. Catapano, G. M. Giannatempo, S. Bonavita, M. Portaluri, M. Tosetti, V. A. d'Angelo, U. Salvolini, G. Tedeschi, Proton MR spectroscopy of cerebral gliomas at 3 T: Spatial heterogeneity, and tumour grade and extent. *Eur. Radiol.* **18**, 1727–1735 (2008).

32. M. N. Hasan, L. Luo, D. Ding, S. Song, M. I. H. Bhuiyan, R. Liu, L. M. Foley, X. Guan, G. Kohanbash, T. K. Hitchens, M. G. Castro, Z. Zhang, D. Sun, Blocking NHE1 stimulates glioma tumor immunity by restoring OXPHOS function of myeloid cells. *Theranostics* **11**, 1295–1309 (2021).
33. A. V. Makela, J. M. Gaudet, P. J. Foster, Quantifying tumor associated macrophages in breast cancer: A comparison of iron and fluorine-based MRI cell tracking. *Sci. Rep.* **7**, 42109 (2017).
34. A. V. Makela, P. J. Foster, Imaging macrophage distribution and density in mammary tumors and lung metastases using fluorine-19 MRI cell tracking. *Magn. Reson. Med.* **80**, 1138–1147 (2018).
35. O. C. Olson, H. Kim, D. F. Quail, E. A. Foley, J. A. Joyce, Tumor-associated macrophages suppress the cytotoxic activity of antimitotic agents. *Cell Rep.* **19**, 101–113 (2017).
36. A. Leftin, N. Ben-Chetrit, J. A. Joyce, J. A. Koutcher, Imaging endogenous macrophage iron deposits reveals a metabolic biomarker of polarized tumor macrophage infiltration and response to CSF1R breast cancer immunotherapy. *Sci. Rep.* **9**, 857 (2019).
37. A. Khurana, F. Chapelin, H. Xu, J. R. Acevedo, A. Molinolo, Q. Nguyen, E. T. Ahrens, Visualization of macrophage recruitment in head and neck carcinoma model using fluorine-19 magnetic resonance imaging. *Magn. Reson. Med.* **79**, 1972–1980 (2018).
38. A. R. Pombo Antunes, I. Scheyltjens, F. Lodi, J. Messiaen, A. Antoranz, J. Duerinck, D. Kancheva, L. Martens, K. De Vlaminck, H. Van Hove, S. S. Kjølner Hansen, F. M. Bosisio, K. Van der Borght, S. De Vleeschouwer, R. Sciot, L. Bouwens, M. Verfaillie, N. Vandamme, R. E. Vandenbroucke, O. De Wever, Y. Saeys, M. Guilliams, C. Gysemans, B. Neyns, F. De Smet, D. Lambrechts, J. A. Van Ginderachter, K. Movahedi, Single-cell profiling of myeloid cells in glioblastoma across species and disease stage reveals macrophage competition and specialization. *Nat. Neurosci.* **24**, 595–610 (2021).
39. C. D. Arvanitis, G. B. Ferraro, R. K. Jain, The blood-brain barrier and blood-tumour barrier in brain tumours and metastases. *Nat. Rev. Cancer* **20**, 26–41 (2020).
40. P. Bouvain, V. Flocke, W. Kramer, R. Schubert, J. Schrader, U. Flogel, S. Temme, Dissociation of ^{19}F and fluorescence signal upon cellular uptake of dual-contrast perfluorocarbon nanoemulsions. *MAGMA* **32**, 133–145 (2019).
41. A. Zomer, D. Croci, J. Kowal, L. van Gurp, J. A. Joyce, Multimodal imaging of the dynamic brain tumor microenvironment during glioblastoma progression and in response to treatment. *iScience* **25**, 104570 (2022).
42. C. Carmona-Fontaine, M. Deforet, L. Akkari, C. B. Thompson, J. A. Joyce, J. B. Xavier, Metabolic origins of spatial organization in the tumor microenvironment. *Proc. Natl. Acad. Sci. U.S.A.* **114**, 2934–2939 (2017).
43. C. N. Parkhurst, G. Yang, I. Ninan, J. N. Savas, J. R. Yates 3rd, J. J. Lafaille, B. L. Hempstead, D. R. Littman, W.-B. Gan, Microglia promote learning-dependent synapse formation through brain-derived neurotrophic factor. *Cell* **155**, 1596–1609 (2013).
44. C. Chirizzi, D. De Battista, I. Tirotta, P. Metrangolo, G. Comi, F. B. Bombelli, L. Chaabane, Multispectral MRI with dual fluorinated probes to track mononuclear cell activity in mice. *Radiology* **291**, 351–357 (2019).
45. U. Flögel, S. Temme, C. Jacoby, T. Oerther, P. Keul, V. Flocke, X. Wang, F. Bonner, F. Nienhaus, K. Peter, J. Schrader, M. Grandoch, M. Kelm, B. Levkau, Multi-targeted ^{1}H/^{19}F MRI unmasks specific danger patterns for emerging cardiovascular disorders. *Nat. Commun.* **12**, 5847 (2021).
46. M. Puchala, Z. Szweda-Lewandowska, J. Kiefer, The influence of radiation quality on radiation-induced hemolysis and hemoglobin oxidation of human erythrocytes. *J. Radiat. Res.* **45**, 275–279 (2004).
47. W. B. Rittase, J. M. Muir, J. E. Slaven, R. M. Bouten, M. A. Bylicky, W. L. Wilkins, R. M. Day, Deposition of iron in the bone marrow of a murine model of hematopoietic acute radiation syndrome. *Exp. Hematol.* **84**, 54–66 (2020).
48. K. Zormpas-Petridis, N. P. Jerome, M. D. Blackledge, F. Carceller, E. Poon, M. Clarke, C. M. McErlean, G. Barone, A. Koers, S. J. Vaidya, L. V. Marshall, A. D. J. Pearson, L. Moreno, J. Anderson, N. Sebire, K. McHugh, D. M. Koh, Y. Yuan, L. Chesler, S. P. Robinson, Y. Jamin, MRI imaging of the hemodynamic vasculature of neuroblastoma predicts response to antiangiogenic treatment. *Cancer Res.* **79**, 2978–2991 (2019).
49. H. G. Wirsching, U. Roelcke, J. Weller, T. Hundsberger, A. F. Hottinger, R. von Moos, F. Caparrotti, K. Conen, L. Remonda, P. Roth, A. Ochsenbein, G. Tabatabai, M. Weller, MRI and ^{18}FET-PET predict survival benefit from bevacizumab plus radiotherapy in patients with isocitrate dehydrogenase wild-type glioblastoma: Results from the randomized ARTE trial. *Clin. Cancer Res.* **27**, 179–188 (2021).
50. I. Dregely, D. Prezzi, C. Kelly-Morland, E. Roccia, R. Neji, V. Goh, Imaging biomarkers in oncology: Basics and application to MRI. *J. Magn. Reson. Imaging* **48**, 13–26 (2018).
51. M. C. Ku, S. Waiczies, T. Niendorf, A. Pohlmann, Assessment of blood brain barrier leakage with gadolinium-enhanced MRI. *Methods Mol. Biol.* **1718**, 395–408 (2018).
52. M. Molgora, M. Colonna, Turning enemies into allies-reprogramming tumor-associated macrophages for cancer therapy. *Med (N Y)* **2**, 666–681 (2021).
53. M. Gromeier, M. C. Brown, G. Zhang, X. Lin, Y. Chen, Z. Wei, N. Beaubier, H. Yan, Y. He, A. Desjardins, J. E. Herndon 2nd, F. S. Varn, R. G. Verhaak, J. Zhao, D. P. Bolognesi, A. H. Friedman, H. S. Friedman, F. McSherry, A. M. Muscat, E. S. Lipp, S. K. Nair, M. Khasraw, K. B. Peters, D. Randazzo, J. H. Sampson, R. E. McLendon, D. D. Bigner, D. M. Ashley, Very low mutation burden is a feature of inflamed recurrent glioblastomas responsive to cancer immunotherapy. *Nat. Commun.* **12**, 352 (2021).
54. N. C. Swinburne, J. Schefflein, Y. Sakai, E. K. Oermann, J. J. Titano, I. Chen, S. Tadayon, A. Aggarwal, A. Doshi, K. Nael, Machine learning for semi-automated classification of glioblastoma, brain metastasis and central nervous system lymphoma using magnetic resonance advanced imaging. *Ann. Transl. Med.* **7**, 232 (2019).
55. K. Niesel, M. Schulz, J. Anthes, T. Alekseeva, J. Macas, A. Salamero-Boix, A. Mockl, T. Oberwahrenbrock, M. Lolies, S. Stein, K. H. Plate, Y. Reiss, F. Rödel, L. Sevenich, The immune suppressive microenvironment affects efficacy of radio-immunotherapy in brain metastasis. *EMBO Mol. Med.* **13**, e13412 (2021).
56. C. Gonzales, H. A. Yoshihara, N. Dilek, J. Leignadier, M. Irving, P. Mieville, L. Helm, O. Michielin, J. Schwitter, In-vivo detection and tracking of T cells in various organs in a melanoma tumor model by 19F-fluorine MRS/MRI. *PLOS ONE* **11**, e0164557 (2016).
57. E. T. Ahrens, B. M. Helfer, C. F. O'Hanlon, C. Schirda, Clinical cell therapy imaging using a perfluorocarbon tracer and fluorine-19 MRI. *Magn. Reson. Med.* **72**, 1696–1701 (2014).
58. S. Weibel, T. C. Basse-Luesebrink, M. Hess, E. Hofmann, C. Seubert, J. Langbein-Laugwitz, I. Gentschev, V. J. Sturm, Y. Ye, T. Kampf, P. M. Jakob, A. A. Szalay, Imaging of intratumoral inflammation during oncolytic virotherapy of tumors by 19F-magnetic resonance imaging (MRI). *PLOS ONE* **8**, e56317 (2013).
59. R. B. van Heeswijk, J. De Blois, G. Kania, C. Gonzales, P. Blyszczuk, M. Stuber, U. Eriksson, J. Schwitter, Selective in vivo visualization of immune-cell infiltration in a mouse model of autoimmune myocarditis by fluorine-19 cardiac magnetic resonance. *Circ. Cardiovasc. Imaging* **6**, 277–284 (2013).
60. E. Darcot, R. Colotti, M. Pellegrin, A. Wilson, S. Siegert, K. Bouzourene, J. Yerly, L. Mazzolai, M. Stuber, R. B. van Heeswijk, Towards quantification of inflammation in atherosclerotic plaque in the clinic - characterization and optimization of fluorine-19 MRI in mice at 3 T. *Sci. Rep.* **9**, 17488 (2019).
61. A. Balducci, Y. Wen, Y. Zhang, B. M. Helfer, T. K. Hitchens, W. S. Meng, A. K. Wesa, J. M. Janjic, A novel probe for the non-invasive detection of tumor-associated inflammation. *Onco. Targets. Ther.* **2**, e23034 (2013).
62. L. Alvaro-Espinosa, A. de Pablos-Aragoneses, M. Valiente, N. Priego, Brain microenvironment heterogeneity: Potential value for brain tumors. *Front. Oncol.* **11**, 714428 (2021).
63. A. A. Mohan, W. H. Tomaszewski, A. P. Haskell-Mendoza, K. M. Hotchkiss, K. Singh, J. L. Reedy, P. E. Fecci, J. H. Sampson, M. Khasraw, Targeting Immunometabolism in Glioblastoma. *Front. Oncol.* **11**, 696402 (2021).
64. S. K. Wculek, G. Dunphy, I. Heras-Murillo, A. Mastrangelo, D. Sancho, Metabolism of tissue macrophages in homeostasis and pathology. *Cell. Mol. Immunol.* **19**, 384–408 (2022).
65. K. Kierdorf, T. Masuda, M. J. C. Jordao, M. Prinz, Macrophages at CNS interfaces: Ontogeny and function in health and disease. *Nat. Rev. Neurosci.* **20**, 547–562 (2019).
66. A. Moore, R. Weissleder, A. Bogdanov Jr., Uptake of dextran-coated monocrystalline iron oxides in tumor cells and macrophages. *J. Magn. Reson. Imaging* **7**, 1140–1145 (1997).
67. C. Zimmer, S. C. Wright Jr., R. T. Engelhardt, G. A. Johnson, C. Kramm, X. O. Breakefield, R. Weissleder, Tumor cell endocytosis imaging facilitates delineation of the glioma-brain interface. *Exp. Neurol.* **143**, 61–69 (1997).
68. H. Konishi, T. Okamoto, Y. Hara, O. Komine, H. Tamada, M. Maeda, F. Osako, M. Kobayashi, A. Nishiyama, Y. Kataoka, T. Takai, N. Udagawa, S. Jung, K. Ozato, T. Tamura, M. Tsuda, K. Yamanaka, T. Ogi, K. Sato, H. Kiyama, Astrocytic phagocytosis is a compensatory mechanism for microglial dysfunction. *EMBO J.* **39**, e104464 (2020).
69. A. DeRosa, A. Leftin, The iron curtain: Macrophages at the interface of systemic and microenvironmental iron metabolism and immune response in cancer. *Front. Immunol.* **12**, 614294 (2021).
70. M. A. Miller, S. Arlauckas, R. Weissleder, Prediction of anti-cancer nanotherapy efficacy by imaging. *Nanotheranostics* **1**, 296–312 (2017).
71. T. Mathivet, C. Bouleti, M. Van Woensel, F. Stanchi, T. Verschuere, L. K. Phng, J. Dejaegher, M. Balcer, K. Matsumoto, P. B. Georgieva, J. Belmans, R. Sciot, C. Stockmann, M. Mazzone, S. De Vleeschouwer, H. Gerhardt, Dynamic stroma reorganization drives blood vessel dysmorphia during glioma growth. *EMBO Mol. Med.* **9**, 1629–1645 (2017).
72. T. N. Phoenix, D. M. Patmore, S. Boop, N. Boulos, M. O. Jacus, Y. T. Patel, M. F. Roussel, D. Finkelstein, L. Goumnerova, S. Perreault, E. Wadhwa, Y. J. Cho, C. F. Stewart, R. J. Gilbertson, Medulloblastoma genotype dictates blood brain barrier phenotype. *Cancer Cell* **29**, 508–522 (2016).
73. K. M. Sullivan, A. Dean, M. M. Soe, OpenEpi: A web-based epidemiologic and statistical calculator for public health. *Public Health Rep.* **124**, 471–474 (2009).
74. C. Dai, J. C. Celestino, Y. Okada, D. N. Louis, G. N. Fuller, E. C. Holland, PDGF autocrine stimulation dedifferentiates cultured astrocytes and induces oligodendrogliomas and oligoastrocytomas from neural progenitors and astrocytes in vivo. *Genes Dev.* **15**, 1913–1925 (2001).

75. L. Sevenich, R. L. Bowman, S. D. Mason, D. F. Quail, F. Rapaport, B. T. Elie, E. Brogi, P. K. Brastianos, W. C. Hahn, L. J. Holsinger, J. Massague, C. S. Leslie, J. A. Joyce, Analysis of tumour- and stroma-supplied proteolytic networks reveals a brain-metastasis-promoting role for cathepsin S. *Nat. Cell Biol.* **16**, 876–888 (2014).
76. W. H. Chae, K. Niesel, M. Schulz, F. Klemm, J. A. Joyce, M. Prummer, B. Brill, J. Bergs, F. Rodel, U. Pilatus, L. Sevenich, Evaluating magnetic resonance spectroscopy as a tool for monitoring therapeutic response of whole brain radiotherapy in a mouse model for breast-to-brain metastasis. *Front. Oncol.* **9**, 1324 (2019).
77. R. Colotti, J. A. M. Bastiaansen, A. Wilson, U. Flogel, C. Gonzales, J. Schwitter, M. Stuber, R. B. van Heeswijk, Characterization of perfluorocarbon relaxation times and their influence on the optimization of fluorine-19 MRI at 3 tesla. *Magn. Reson. Med.* **77**, 2263–2271 (2017).
78. R. Watts, Y. Wang, k-space interpretation of the Rose Model: Noise limitation on the detectable resolution in MRI. *Magn. Reson. Med.* **48**, 550–554 (2002).

Acknowledgments: We thank members of the Joyce Lab for insightful discussion, and M. Massara, L. Tillard, M. Kornete, and S. Rumac for excellent technical support. We are grateful to the In Vivo Imaging Facility and the Flow Cytometry Facility at the University of Lausanne for assistance and advice, particularly A. Benechet and D. Labes, respectively. We thank L. Akkari, NKI, and P.-C. Ho, University of Lausanne, for informative scientific discussions. We also acknowledge the CIBM Center for Biomedical Imaging, founded and supported by CHUV, University of Lausanne, Écôle Polytechnique Fédérale de Lausanne, University of Geneva, and Geneva University Hospitals. Mouse silhouette, syringe, and reference tube drawings in the figures were sourced from https://app.biorender.com/biorender-templates. **Funding:** This research was supported in part by the Swiss Cancer Research Foundation (KFS-3390-08-2016 and KFS-5280-02-2021), Charlie Teo Foundation, Ludwig Institute for Cancer Research, and University of Lausanne (to J.A.J.), the Swiss National Science Foundation (32003B_182615 to R.B.v.H.), the Deutsche Forschungsgemeinschaft (TE1209/1-1 and 1-2; FL303; to S.T. and U.F.), the E. Schrödinger fellowship J4343 by the Austrian Science Fund FWF (to K.S.), a Human Frontier Science Program fellowship (LT000240/2017-L), a Veni fellowship from the Netherlands Organization for Scientific Research (09150161910076 to A.Z.), and the European Union's Horizon 2020 research and innovation program under the Marie Skłodowska–Curie grant agreement (no. 955951, Evomet ITN), which supports R.S.M. **Author contributions:** D.C., R.B.v.H., and J.A.J. conceived the study, designed experiments, and interpreted data. D.C. and J.A.J. wrote the manuscript. D.C., R.S.M., K.S., A.Z., R.C., V.W., and R.B.v.H. performed the experiments. S.T. and U.F. provided materials. D.C. and R.B.v.H. performed the MRI analyses, N.F. performed the RNA-seq analyses, and D.C. performed all other experimental analyses. All authors edited or commented on the manuscript. **Competing interests:** The authors declare that they have no competing interests. D.C. has received consulting fees from Seed Biosciences SA. J.A.J. has received honoraria for speaking at research symposia organized by Bristol Meyers Squibb and Glenmark Pharmaceuticals and currently serves on the scientific advisory board of Pionyr Immunotherapeutics. **Data and materials availability:** All data associated with this study are present in the paper or the Supplementary Materials. The raw RNA-seq data generated in this study are accessible in the GEO under number GSE190109: (www.ncbi.nlm.nih.gov/geo/query/acc.cgi?acc=GSE190109; provisional token: izyhacamlhmvzkl). The scripts used to analyze the MR images can be found at https://wp.unil.ch/cvmr/links/.

Submitted 3 February 2022
Resubmitted 08 July 2022
Accepted 15 September 2022
Published 19 October 2022
10.1126/scitranslmed.abo2952

Science Translational Medicine

Multispectral fluorine-19 MRI enables longitudinal and noninvasive monitoring of tumor-associated macrophages

Davide Croci, Rui Santalla Mndez, Sebastian Temme, Klara Soukup, Nadine Fournier, Anoek Zomer, Roberto Colotti, Vladimir Wischnewski, Ulrich Flgel, Ruud B. van Heeswijk, and Johanna A. Joyce

Sci. Transl. Med., **14** (667), eabo2952.
DOI: 10.1126/scitranslmed.abo2952

Monitoring Monocytes

Tumor-associated microglia and macrophages (TAMs) play a major role in defining disease progression for central nervous system tumors. However, monitoring these cells has historically required invasive biopsies. Here, Croci *et al.* used fluorine isotope 19 magnetic resonance imaging (^{19}F MRI) to noninvasively track TAMs in mice. The authors intravenously injected perfluorocarbon-containing nanoparticles into tumor-bearing mice, finding that they could reliably track TAMs over time and in response to radiotherapy. These findings highlight the potential for ^{19}F MRI as a monitoring strategy for patients with central nervous system tumors.

Science Translational Medicine (ISSN) is published by the American Association for the Advancement of Science. 1200 New York Avenue NW, Washington, DC 20005. The title *Science Translational Medicine* is a registered trademark of AAAS.